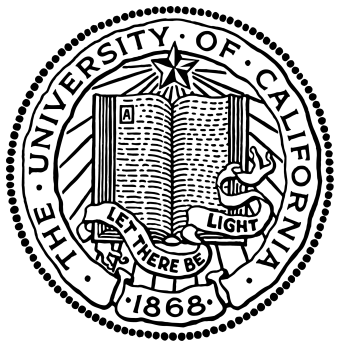

UCSF Department of Radiology and Biomedical Imaging

11th Annual

RADIOLOGY IMAGING RESEARCH SYMPOSIUM

October 21, 2014

Organizers:
Peder Larson, PhD, Jing Liu, PhD, Katherine Murphy, and Brad Nakano

Acknowledgements:
Michael Evans, PhD, K. Pallav Kolli, MD, Roland Krug, PhD, Xiaojuan Li, PhD, Sharmila Majumdar, PhD
Susanne Mueller, PhD, Andrew Phelps, MD, Elissa Price, MD, Viola Rieke, PhD, David Saloner, PhD
Vivek Swarnakar, Duygu Tosun-Turgut, PhD, Khai Vu, MD, Esther Yuh, MD, PhD, Xiaoliang Zhang, PhD

Research Interest Groups

Research Interest Groups (RIGs) bring together departmental PhD and MD research and clinical faculty, as well as trainees across our campuses into synergized research groups. They provide a structure for PhD faculty akin to Clinical Sections for purposes of improving departmental visibility and connection. Each group is typically led by a PhD Director and MD Co-Director, who collectively (with their SRG colleagues) form an Executive Research Council.

Body RIG:
John Kurhanewicz, PhD (Director)
Z. Jane Wang, MD (Co-Director)

Brain RIG:
Sarah J. Nelson, PhD (Director)
Srikantan Nagarajan, PhD (Co-Director)
Pratik Mukherjee, MD, PhD (Co-Director)

Breast Cancer RIG:
Nola Hylton, PhD (Director)
Bonnie N. Joe, MD, PhD (Co-Director)

Cardiovascular RIG:
David Saloner, PhD (Director)
Karen Ordovas, MD (Co-Director)

Musculoskeletal RIG:
Sharmila Majumdar, PhD (Director)
Thomas Link, MD, PhD (Co-Director)

Neurodegenerative RIG:
Pratik Mukherjee MD, PhD (Co-Director)
Norbert Schuff, PhD (Co-Director)

Pediatrics/Fetal RIG:
A. James Barkovich, MD (Director)

Specialized Resource Groups

Specialized Resource Groups (SRGs) bring together departmental PhD and MD research and clinical faculty, who do technique development. Each group is typically led by either a PhD or MD Director, who collectively (with their RIG colleagues) form an Executive Research Council.

Advanced Imaging Technologies SRG:
Dan Vigneron, PhD (Director)

Image-Guided Surgery SRG:
Alastair Martin, PhD (Director)
Mark Wilson, MD (Co-Director)
Steve Hetts, MD (Co-Director)

UCSF Department of Radiology and Biomedical Imaging

The 11th Annual Radiology Imaging Research Symposium

http://www.radiology.ucsf.edu/research/meetings/imaging-research-symposium/2014

October 21, 2014

Registration:
12:30pm, Cole Hall, 513 Parnassus Ave.

Speaker Presentations:
1:00pm – 4:30pm, Cole Hall, 513 Parnassus Ave.

Posters, Awards and Reception:
4:30pm – 5:45pm, Millberry Union, Golden Gate and City Lights Rooms, 500 Parnassus Ave.

Symposium Program

12:30 pm	**Registration & RIG Videos** **Cole Hall**
1:00-1:10 pm	**Opening Remarks** ***Sharmila Majumdar, PhD, Professor and Vice Chair for Research, Department of Radiology and Biomedical Imaging***

Oral Presentations (Session I)
Moderators: Andrew Phelps, MD and Peder Larson, PhD

1:10-1:20 pm	Knee Bone Shape Features Predict the Progression of Cartilage T1ρ 1 Year after ACL Reconstruction *Valentina Pedoia, Favian Su, Drew A. Lansdown, Musa Zaid, Richard Souza, Benjamin C. Ma, Xiaojuan Li*
1:20-1:30 pm	Chemical Exchange Saturation Transfer Imaging of Knee at 3T *Anand K. Venkatachari. Cory Wyatt, Sharmila Majumdar*
1:30-1:40 pm	Optimization of MRI for Breast Cancer Subtypes in Predicting Response to Neoadjuvant Chemotherapy *Wen Li, Wei-Ching Lo, Ella F. Jones, David C. Newitt, John Kornak, Lisa J. Wilmes, Nola M. Hylton*
1:40-1:50 pm	Dynamic 3D Imaging of Mouse Prostate Cancer for Estimation of Metabolic and Perfusion Kinetics *Hsin-Yu Chen, Peder E. Z. Larson, Cornelius von Morze, Christine Leon Swisher, Naeim Bahrami, Robert Bok, John Kurhanewicz, and Daniel B. Vigneron*
1:50-2:00 pm	Hyperpolarized [1-13C] Glutamate: a Metabolic Imaging Biomarker of IDH1 Mutational Status in Glioma *Myriam M. Chaumeil, Peder E.Z. Larson, Sarah M. Woods, Larry Cai, Pia Eriksson, Aaron E. Robinson, Janine M. Lupo, Daniel B. Vigneron, Sarah J. Nelson, Russell O. Pieper, Joanna J. Phillips, Sabrina M. Ronen*
2:00-2:10 pm	Design of an Energy-Independent SPECT Gamma Camera using a CZT Detector and Pixel-Matched Collimator *Srijeeta Bagchi, Fenghua Weng, Qiu Huang, Youngho Seo*

2:10-2:20 pm	H2O2- labile [18F]FLT Prodrug for Sensing ROS in UOK262 Renal Carcinoma Cells *Valerie Carroll, Brian W. Michel, Joseph Blecha, Henry VanBrocklin, Melanie Regan, Justin Delos Santos, Kayvan R. Keshari, Christopher J. Chang, David M. Wilson*
2:20-2:30 pm	Biological Response to Bevacizumab Using FMISO PET/MR Imaging In Recurrent Glioma *Ramon F. Barajas Jr., Miguel H. Pampaloni, Soonmee Cha*
2:30-3:00 pm	**Coffee Break & RIG Videos**

Oral Presentations (Session II)
Moderators: Jing Liu, PhD, and K. Pallav Kolli, MD

3:00-3:10 pm	Selective Deletion of Nociceptors by Ganglionic Injection of Resiniferatoxin *Jacob Brown, Maythem Saeed, Michael Iadarola, Alan Basbaum, Loi Do, Mark Wilson, Steve Hetts, Bill Dillon*
3:10-3:20 pm	Anatomic Embedding of the Structural Connectome Within the Human Brain *Julia Owen, YiShin Chang, Pratik Mukherjee*
3:20-3:30 pm	Regional Functional Connectivity Predicts Distinct Cognitive Impairments in Alzheimer's Spectrum *Kamalini G. Ranasinghe, Leighton B. Hinkley, Alexander J. Beagle, Danielle Mizuiri, Anne F. Dowling, Susanne M. Honma, Mariel M. Finucane, Carole Scherling, Bruce L. Miller, Srikantan S. Nagarajan, Keith A. Vossel*
3:30-3:40 pm	Variability of Resting-State Cortical Functional Connectivity In Hypoxic-Ischemic Infants *Trevor Flynn, Srivathsa Veeraraghavan, Donna Ferriero, A. James Barkovich, Duan Xu*
3:40-3:50 pm	MRI Quantification of Function, Perfusion and Viability in Microembolized Ischemic Myocardium *Loi Do, Skylar Nahi, Brenda Zheng, Mark Wilson, Maythem Saeed*
3:50-4:00 pm	FID Navigator for Motion Compensation in 3D Black Blood Carotid MRI *Henrik Haraldsson, Sinyeob Ahn, Chengcheng Zhu, David Saloner*
4:00-4:10 pm	Ultrasound Findings in Failed Pancreas Transplants *Tara A. Morgan, Vickie A. Feldstein, Jack Harbell, Peter G. Stock, Rebecca Smith-Bindman*
4:10-4:20 pm	Development of Endovascular Chemotherapy Filter for Removing Doxorubicin from Blood: In Vivo Study *Jeffrey Yang, Chia-Hung Sze, Anand S. Patel, Maythem Saeed, Daniel L. Cooke, Albert K. Chin, Mark W. Wilson, Steven W. Hetts*
4:30-6:00 pm	**Poster Session, Award Presentations, and Reception** **Millberry Union**
4:45 pm	**Presentation of the Hasegawa Award** ***David Saloner, PhD*** ***Professor in Residence, Dept of Radiology and Biomedical Imaging***
5:45 pm	**Podium and Poster Presentation Awards** ***Xiaojuan Li, PhD*** ***Associate Professor in Residence, Dept of Radiology and Biomedical Imaging***
5:50 pm	**Closing Comments** ***Ronald L. Arenson, MD*** ***Professor and Chair, Department of Radiology and Biomedical Imaging***

Oral Presentations

Knee bone shape features predict the progression of cartilage T1ρ 1 year after ACL reconstruction

Valentina Pedoia, Favian Su, Drew A. Lansdown, Musa Zaid, Richard Souza, Benjamin C. Ma, Xiaojuan Li

Presenting Author
Name: Valentina Pedoia
Email: valentina.pedoia@ucsf.edu
Presenting Author's RIG/SRG: Musculoskeletal
Presenting Author's Lab Location: China Basin

Senior Author
Name: Xiaojuan Li
Email: xiaojuan.li@ucsf.edu

Abstract highlights: The results of this study suggest that specific aspects of the tibia shape can predict the progression of T1ρ 1 year after ACL reconstruction. Understanding the interrelationship between the knee shape and signs of early cartilage changes may help with better understanding post-traumatic OA development in ACL reconstructed knees.

Introduction: ACL tears are a well-known risk factor for the development of early post-traumatic osteoarthritis (OA) Previous studies have demonstrated T1ρ MRI quantification can detect cartilage damage and early degeneration after ACL injury and reconstruction. Recently, bone shape features have been proposed as potential markers for predicting hip and knee OA progression. However, the potential role of bone shape in post-traumatic OA development after ACL injury is unknown. In the present study, 3D Statistical Shape modeling (SSM) is applied to explore the relationship between knee bone shape and the progression of cartilage T1ρ 1 year after ACL reconstruction.

Methods: Bilateral knees were scanned using a 3 Tesla MRI scanner (GE Healthcare, Milwaukee, WI, USA) with an 8-channel phased array knee coil (Invivo, Orlando, FL, USA) for thirty-six patients with ACL injuries prior to surgical reconstruction (age = 28.56 ± 7.46 years, BMI = 23.69± 2.75 kg/m2, 15 female) and 1 year after reconstruction. The imaging protocol included: (1) sagittal T2 fast spin-echo (FSE) images, slice thickness of 1.5 mm, spacing of 1.5 mm, field of view of 16 cm, 512 x 512 matrix size (2) high-resolution 3D FSE (CUBE), field of view of 16 cm matrix 384 x 384 matrix size, slice thickness 0.5 mm; (3) quantitative T1ρ: TSL = 0/10/40/80 ms,slice thickness 4 mm, field of view of 14 cm, 256 × 128 matrix size. Sagittal CUBE images were used for the cartilage segmentation. Six compartments were identified: medial femoral condyle (MFC), medial tibia (MT), lateral femoral condyle (LFC) and lateral tibia (LT) trochlea (TRO) and patella (PAT). T1ρ relaxation times were determined with a pixel-by-pixel, two-parameter exponential fit and averaged in each compartment. The difference between the T1ρ in each compartment is computed as: T1ρ_1year - T1ρ _baseline. The tibia and femur are segmented semi-automatically on the FSE image. Landmarks are defined with a correspondence algorithm based on the local curvature and used for SSM extraction. The first 20 modes which represent more than 90% of the entire variability, were analyzed. Femur and tibia modes are considered as possible predictor of the T1ρ progression in a stepwise linear regression.

Results: Good prediction models were found for LT ($R^2 = 0.4$ $p<0.001$), MFC ($R^2 = 0.4$ $p<0.001$) and MT ($R^2 = 0.33$ $p=0.013$). Interestingly T16 is present in all 3 models and is the one with the highest weight for both MFC and LT models. Discussion: In Figure 1, a model of the deformation equal to mean – 3SD of the mode T16 is shown. The correlation between T1ρ progression and T16 is negative for all the 3 cartilage compartments. The maximum of the vertices' displacement is in the inferior to superior direction Significant deformation is present in both the posteromedial and anterolateral portion.

Conclusion: Understanding the interrelationship between the knee shape in the ACL reconstructed knee and signs of early cartilage changes may help with better understanding post-traumatic OA development in ACL reconstructed knees and ultimately help with improving patient management.

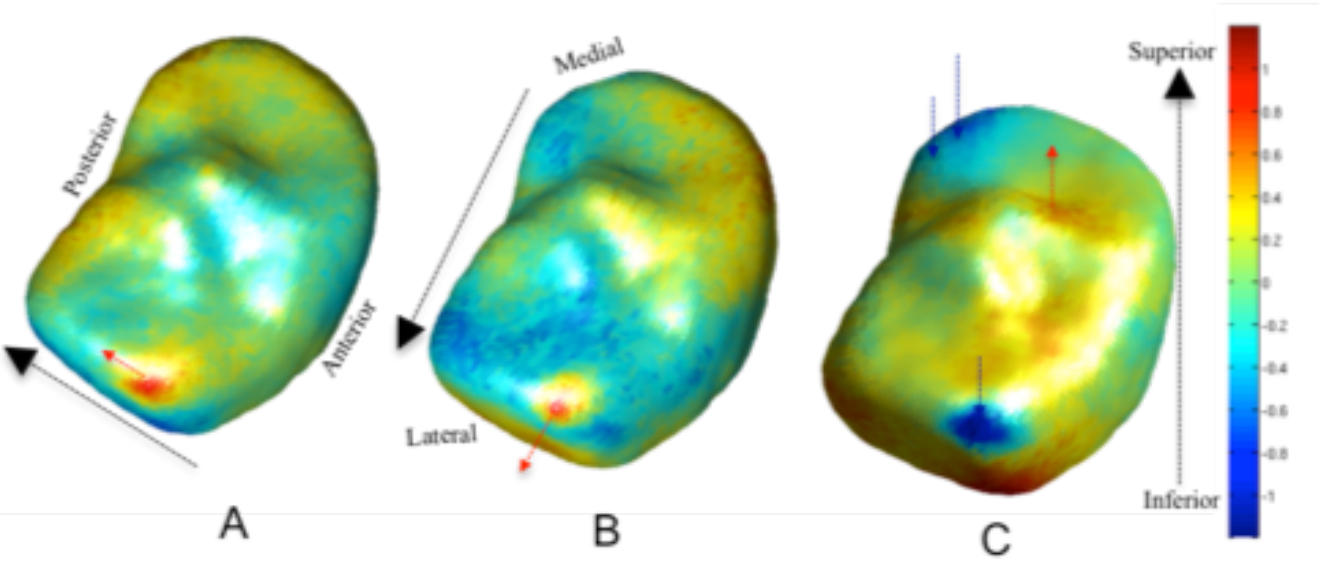

Figure 1 3D representation of the vertices displacement modeling the main bone shape features that can predict MFC, MT and LFC $T_{1\rho}$ progression.

A) Anterior to posterior: positive values (red) displacement towards posterior direction, negative values (blue) displacement towards anterior direction, B) medial to lateral: positive values (red) displacement towards lateral direction, negative values (blue) displacement towards medial direction C) inferior to superior: positive values (red) displacement towards superior direction, negative values (blue) displacement towards inferior direction.

Chemical Exchange Saturation Transfer Imaging of Knee at 3T

Anand K. Venkatachari. Cory Wyatt, Sharmila Majumdar

Presenting Author
Name: Anand Venkatachari
Email: Anand.venkatachari@ucsf.edu
Presenting Author's RIG/SRG: Musculoskeletal
Presenting Author's Lab Location: China Basin

Senior Author
Name: Sharmila Majumdar
Email: Sharmila.majumdar@ucsf.edu

Abstract highlights: Osteoarthritis affects millions of people around the world. It is believed that the onset of Osteoarthritis is due to the loss of proteoglycans in the cartilage tissue. We have developed Chemical Exchange Saturation Transfer sequence for looking at glycosaminoglycan, which are side chains attached to the core proteins of proteoglycans.

Introduction: Chemical Exchange Saturation Transfer (CEST) imaging of the Glycosaminoglycan (GAG) in the cartilage can be used for early detection of Osteoarthritis. Every GAG unit has one Amide (–NH) and three Hydroxyl (–OH) groups which can be used for CEST imaging. In cartilage, Hydroxyl protons are used for CEST imaging (GagCEST). The Hydroxyl protons resonate between +0.9 to +1.9 PPM from Water peak. In GagCEST imaging the Hydroxyl protons are saturated at their resonance frequency. The saturation is transferred to bulk water and can be visible on the water signal. Asymmetric Magnetization Transfer Ratios (MTRasym) is computed to eliminate the effect of Direct Water Saturation (DS) and Magnetization Transfer (MT).

Methods: CEST sequence is developed using segmented 3D Spoiled Gradient Echo (SPGR) sequence. The CEST segment consists of a train of Saturation Pulses followed by segmented 3D SPGR acquisition. 5 Gaussian pulses each 80ms in duration and an inter-pulse duration of 10ms was used for CEST imaging. Gradients were applied between the Pulses to eliminate residual transverse magnetization. CEST is sensitive to B0 inhomogeneity and to correct for field inhomogeneity 3D SPGR with IDEAL (3 point Dixon) was acquired to generate the B0 map. All the scans were done on 3T Signa Discovery wide Scanner (GE Healthcare Technologies, Milwaukee, WI, USA) using 8 Channel T/R Knee coil. The sequence parameters for CEST sequence were FOV 140cm; Resolution 256*128; Slice Thickness 4mm; #Slices 20; Flip Angle 10; BW 31.2KHz. Frequency offsets +2 PPM to +0.5 PPM and -0.5 PPM to -2 PPM in the increments of 0.1 PPM and one with CEST pulse OFF; TR 6ms; TE 3ms; Number of slices 20; Scan time 10 minutes. All the frequency-offset images were registered against Water images generated from IDEAL scan to account for motion. The Water image was used for segmenting the cartilage. Each pixel in the cartilage was corrected for B0 inhomogeneity by using B0 field map. MTR maps are computed by integrating between 1 to 1.5 PPM. All the processing was done using custom developed MATLAB scripts. The Asymmetric Magnetization Transfer Ratio is computed as follows: $MTRasym = (S(-\Delta\omega) - S(+\Delta\omega))/S0 *100$

Results: Water saturation shift referencing (WASSR) technique is used for B0 Correction with CEST. WASSR is the gold standard but the acquisition is very long. In the current study we have compared the B0 map generated between WASSR and IDEAL. The B0 map from IDEAL matches very well with WASSR (Figure 1) and the acquisition time with IDEAL is less than 2 minutes. The B0 inhomogeneity is less than ±0.5 PPM in all the volunteers tested (Figure 2). The CEST scan were acquired to account for ±0.5 PPM B0 inhomogeneity. RF power for the CEST pulses was optimized and CEST maps were generated in healthy volunteers (Figure 3). The average MTR was less than 1%, which is in agreement with literature.

Conclusion: In the current study we have developed a CEST protocol that can be acquired in less than 12 minutes with B0 field correction.

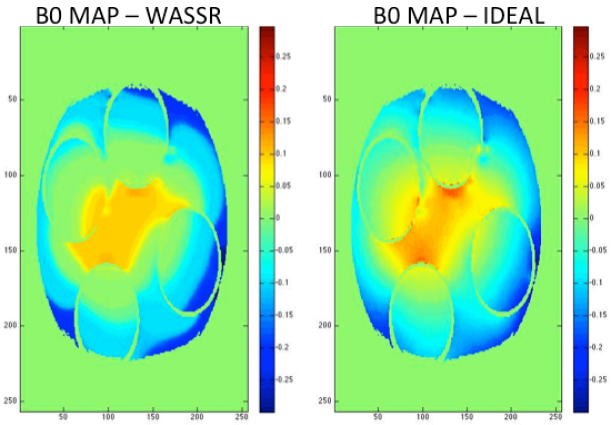

Figure 1: B0 MAP WASSR vs. IDEAL

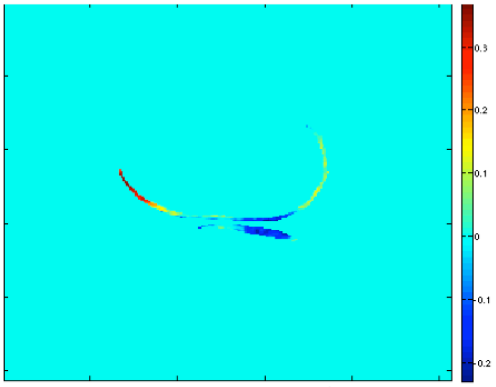

Figure 2: B0 MAP in Volunteer

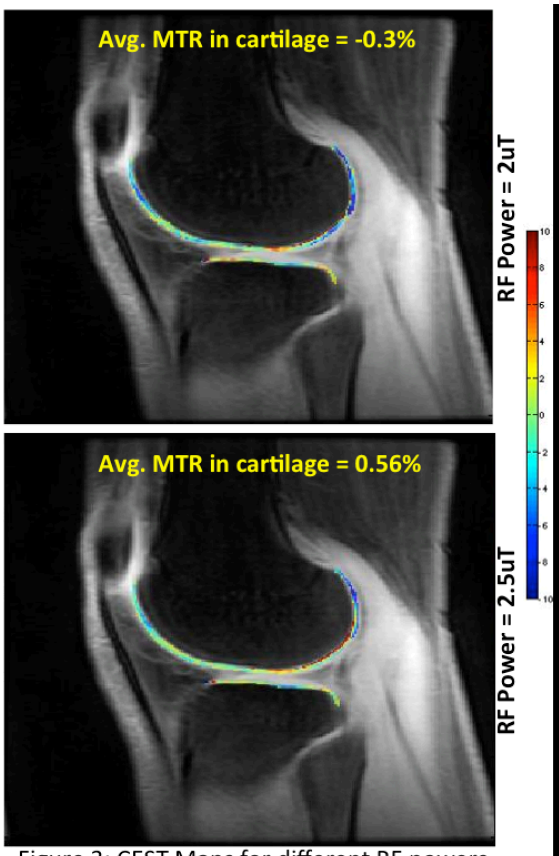

Figure 3: CEST Maps for different RF powers

Optimization of MRI for Breast Cancer Subtypes in Predicting Response to Neoadjuvant Chemotherapy

Wen Li, Wei-Ching Lo, Ella F. Jones, David C. Newitt, John Kornak, Lisa J. Wilmes, Nola M. Hylton

Presenting Author
Name: Wen Li
Email: wen.li@ucsf.edu
Presenting Author's RIG/SRG: Breast Cancer MRI/MRS
Presenting Author's Lab Location: Mount Zion

Senior Author
Name**:** Nola Hylton
Email: nola.hylton@ucsf.edu

Abstract highlights: This study was undertaken to explore the significance of functional tumor volume for predicting breast cancer recurrence following neoadjuvant chemotherapy. Our finding suggests that performance of imaging predictors based on FTV may be improved if threshold optimization is performed separately for the clinically-relevant subtypes defined by hormone receptor status.

Introduction: Change in functional tumor volume (FTV) measured by dynamic contrast-enhanced magnetic resonance imaging (DCE-MRI), has been shown to be associated with response to neoadjuvant chemotherapy (NACT) for patients with stage II/III breast cancer. FTV reflects the vascularized volume of tumor and is calculated by applying minimum thresholds PEt for the initial percent enhancement and SERt for the early-to-late signal enhancement ratio following gadolinium contrast injection. In this retrospective study, we investigate the association of FTV influenced by PEt and SERt values with recurrence-free survival (RFS) in breast cancer subtypes defined by hormone receptor (HR) and HER2 status.

Methods: 64 patients with locally advanced breast cancer were imaged by DCE-MRI before treatment (MRI1), after one cycle of adriamycin-cytoxan (AC) therapy (MRI2), inter-regimen (MRI3, taxane receivers only) and at the completion of chemotherapy prior to surgery (MRI4). Because treatment length and regimen varied among patients, the MRI exam performed after all NACT and before surgery was designated as final MRI (MRIf). FTV was calculated with varying PEt (30–200% in steps of 10%) and SERt (0–2 in steps of 0.2) values. A Cox proportional hazard model was used to analyze association with RFS, defined as the time between surgery and disease recurrence or last disease-free follow-up, for the following imaging predictors: early percent change in FTV (ΔFTV2: MRI1 vs. MRI2), final percent change (ΔFTVf: MRI1 vs. MRIf), and final FTV (FTVf). RFS association was evaluated for the full cohort and within subsets defined by tumor subtype (HR+/HER2-, HER2+, triple negative). Estimated hazard ratios per unit change in predictors, associated 95% confidence intervals (CI) and p-values were evaluated. The cutoff of $p<0.05$ was used to differentiate PEt/SERt values with higher predictive performance.

Results: For the full cohort, FTVf showed the most robust association with RFS among the three predictors, with $p<0.05$ across all measured combinations of PEt/SERt. The PEt/SERt combination with smallest p-value was found for PE=30% and SER=0.2, with hazard ratio 1.09 (95% CI 1.06−1.13, $p<0.001$). P-values less than 0.05 for the ΔFTVf predictor was found for the full range of SERt values tested, but was mostly confined to PEt in 30−110% range; ΔFTV2 resulted in $p<0.05$ for very few PEt/SERt combinations. When analyzed by tumor subtypes, different prediction profiles were observed. FTVf showed $p<0.05$ for the lower PEt range only in the HER2+ (n=15) and triple-negative (n=11) groups. A limited number of PEt/SERt pairs showed $p<0.05$ for ΔFTVf and ΔFTV2, with the exception of the ΔFTVf in the triple-negative group, for which $p <0.05$ for many PEt/SERt combinations in the low PEt range.

Conclusion: This study was undertaken to explore the significance of FTV for predicting breast cancer recurrence following NACT. While this study is retrospective in nature and had small sample size, the findings nevertheless suggest that performance of imaging predictors based on FTV may be improved if threshold optimization is performed separately for the clinically-relevant subtypes defined by HR and HER2 receptor expression.

Dynamic 3D Imaging of Mouse Prostate Cancer for Estimation of Metabolic and Perfusion Kinetics

Hsin-Yu Chen, Peder E. Z. Larson, Cornelius von Morze, Christine Leon Swisher, Naeim Bahrami, Robert Bok, John Kurhanewicz, and Daniel B. Vigneron

Presenting Author
Name: Hsin-Yu Chen
Email: hsin-yu.chen@ucsf.edu
Presenting Author's RIG/SRG: Prostate Cancer
Presenting Author's Lab Location: Mission Bay

Senior Author
Name: Dan Vigneron
Email: Dan.vigneron@ucsf.edu

Abstract highlights: Simultaneous imaging of metabolism and perfusion in mouse prostate cancer was studied using a novel high spatiotemporal resolution 3D dynamic compressed sensing sequence. Quantitative analysis of dynamics in vivo using a two-site exchange models was performed to investigate prostate cancer aggressiveness.

Introduction: MR imaging with hyperpolarized 13C substrates can increase the SNR by more than 10,000 fold. Such improvement promotes rapid visualization of metabolic pathways and perfusion kinetics in vivo. Discriminating between the aggressive and indolent forms has been the Holy Grail in the diagnostics of prostate cancer, as no existing imaging marker confidently provides such assessments. However, aggressive prostate tumor demonstrates significantly increased metabolic conversion from pyruvate to lactate due to genetic mutations resulting in upregulated lactate-dehydrogenase (LDH). Concomitantly, vasculature and perfusion patterns are also altered. In this study, we developed a novel 3D dynamic MRI acquisition method using co-hyperpolarized [1-13C]pyruvate and [13C]urea to detect metabolism and perfusion simultaneously on transgenic prostate cancer mouse model (TRAMP) with the goal of characterizing the aggressiveness of prostate cancer.

Methods: Pulse Sequence: A 3D dynamic MRSI sequence was designed to acquire the metabolic and perfusion imaging data. The acquisition featured a spectral-spatial RF excitation optimized for dynamic imaging, followed by a double spin-echo refocusing and EPSI readout with random undersampling blips. (spectral BW= 581Hz, spectral res= 9.83Hz, FOV=4x4x8.6cm3, res= 3.3x3.3x5.4mm3) The random in-plane undersampling and a compressed sensing reconstruction provided rapid time-series acquisitions with 2s temporal resolution. Hyperpolarization and Imaging Experiments: In this project, transgenic mice (N=10) with prostate cancer (TRAMP model) were studied. [13C]Pyruvate and [13C]urea was co-polarized using a prototype 3.35T clinical polarizer in development with GE Healthcare. A volume of 350ul of 80mM co-polarized pyruvate and urea solution (30~40% polarization) was administered over 15 seconds through tail vein and the image acquisition started at the end of injection.

Results: Kinetic fitting using compartmental exchange models provided quantitative analysis for the rates of biochemical processes and perfusion of [13C] markers in tumor tissue. Pyruvate-to-lactate conversion and perfusion rates (N=10) in aggressive tumors were k_pl = 0.0541±0.0100 and k_trans = 1762.4±1258.7 (ml/dL/min), respectively, as opposed to k_pl = 0.0208±0.0039 and k_trans =466.4±301.73(ml/dL/min) in early stage ones.

Conclusion: With the novel sequence and modeling methods, we were able to demonstrate from our data that metabolism and perfusion has high correlation with histochemical grading of mouse prostate cancer. In this study, k_pl measurements were significantly higher (~2-fold) in aggressive late stage prostate tumors vs. early stage and accompanied by decrease in perfusion index k_trans.

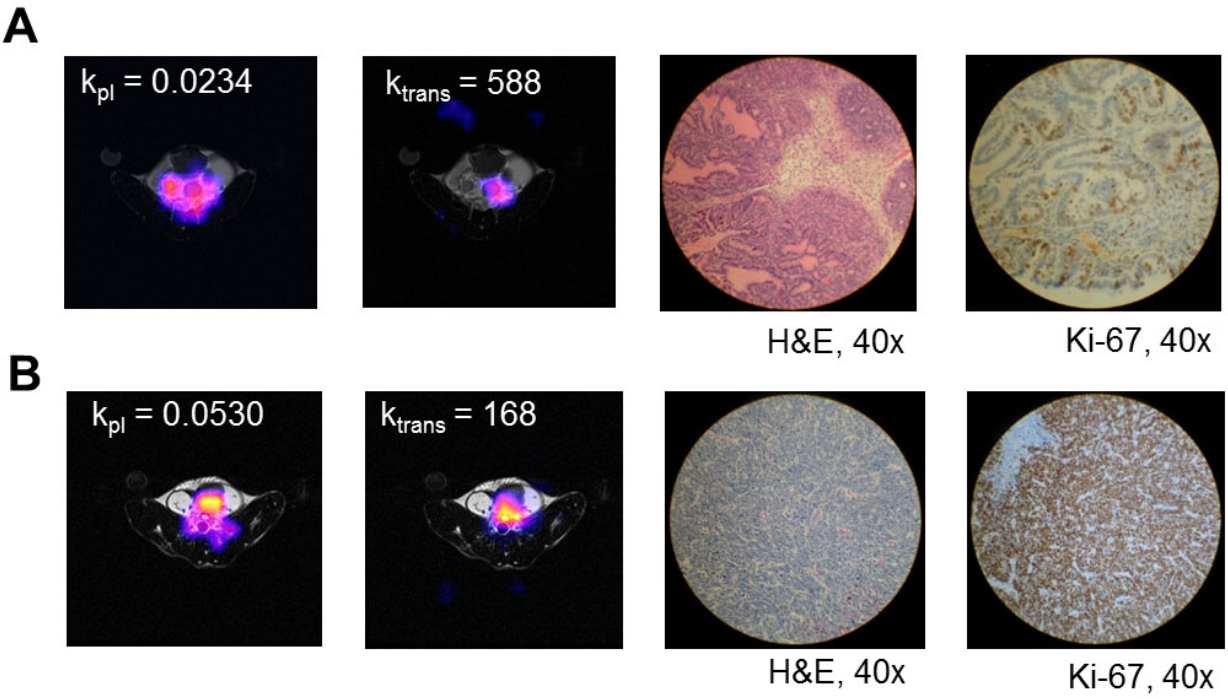

Fig.1 Quantitative metrics of metabolism and perfusion in two TRAMPs (**A** and **B**). The k_{pl} and k_{trans} maps, compared to histopathological analysis, suggest that metabolism and perfusion/permeability reflects fundamental pathophysiology in TRAMP mouse model of prostate cancer. In general, TRAMP prostate tumor shows elevated metabolism and altered perfusion/permeability versus normal tissue.

Hyperpolarized [1-13C] glutamate: a metabolic imaging biomarker of IDH1 mutational status in glioma

Myriam M. Chaumeil, Peder E.Z. Larson, Sarah M. Woods, Larry Cai, Pia Eriksson, Aaron E. Robinson, Janine M. Lupo, Daniel B. Vigneron, Sarah J. Nelson, Russell O. Pieper, Joanna J. Phillips, Sabrina M. Ronen

Presenting Author
Name: Myriam Chaumeil
Email: myriam.chaumeil@ucsf.edu
Presenting Author's RIG/SRG: Brain Cancer MRI/MRS
Presenting Author's Lab Location: Mission Bay

Senior Author
Name: Sabrina Ronen
Email: sabrina.ronen@ucsf.edu

Abstract highlights: Hyperpolarized glutamate is a new metabolic imaging biomarker that informs on mutant IDH1-associated metabolic changes mediating decreased glutamate production

Introduction: Mutations of the isocitrate dehydrogenase 1 (IDH1) gene are among the most prevalent in low-grade glioma and secondary glioblastoma, represent an early pathogenic event, and are associated with epigenetically-driven modulations of metabolism. Of particular interest is the recently uncovered relationship between IDH1 mutation and decreased activity of the branched-chain amino acid transaminase 1 (BCAT1) enzyme. Non-invasive imaging methods that can assess BCAT1 activity could therefore improve detection of mutant IDH1 tumors and aid in developing and monitoring new targeted therapies. BCAT1 catalyzes the transamination of branched-chain amino acids while converting α-ketoglutarate (α-KG) to glutamate. Our goal was to use 13C magnetic resonance spectroscopy to probe the conversion of hyperpolarized [1-13C] α-KG to glutamate as a readout of BCAT1 activity.

Methods: Cells U87 GBM cells were transduced with a viral vector coding for wild-type (U87IDHwt) or mutant IDH enzyme (U87IDHmut). For bioreactors experiments, 3x107 cells were grown on microcarrier beads and loaded into a 10-mm NMR tube connected to a perfusion system. Animals Orthotopic tumors were implanted in athymic rats by injecting a suspension of cells (~3x105 in 10μL) in the right caudate. A 23G catheter was secured in the tail vein. Hyperpolarized α-KG [1-13C] αKG (5.9M) was polarized using a Hypersense polarizer for 1h, dissolved in buffered solutions and rapidly injected either into perfused cells (15mM) or intravenously in animals (100mM). 13C MRS Perfused cells: Dynamic sets of 13C spectra were acquired on a 500-MHz INOVA spectrometer (Agilent Technologies) using 13deg pulses and 3sec TR. In vivo: 2D dynamic 13C data were acquired on a 3T MR system (GE Healthcare) using a multi-band variable flip-angle scheme optimized for detection of HP glutamate. Cell 13C spectra were quantified using ACD/Spec Manager and Gamma-variate (GVA) was performed. In vivo data were processed using the in-house SIVIC software. Activity assays The enzymatic activity of BCAT1, alanine transaminase ALT, glutamate dehydrogenase GDH and aspartate aminotransferase AST1 were measured in U87IDHmut and U87IDHwt cells using spectrophotometric assays.

Results: Injection of HP αKG in U87IDHwt cells resulted in a significant build-up of HP [1-13C] glutamate, whereas HP glutamate was barely detectable in U87IDHmut cells (Fig. A-C). Following injection of HP αKG in tumor-bearing animals, HP glutamate was detected in the U87IDHwt tumor only, not in U87IDHmut, in line with the cells results (Fig. E-F). Mechanistically, we demonstrated that the observed drop in HP glutamate in U87IDHmut cells and tumors was likely mediated not only by a drop in BCAT1 activity (Fig G), but also by reductions in aspartate transaminase and glutamate dehydrogenase activities (Fig. H), suggesting additional metabolic reprogramming associated with IDH1 mutation.

Conclusion: Collectively, our findings indicate that HP glutamate production from HP αKG can be detected in perfused cells and in vivo using 13C MRS, and is decreased in U87IDHmut cells/tumors. HP glutamate could thus potentially serve as a non-invasive surrogate marker of IDH1 mutational status in gliomas.
Acknowledgements: NIH R21CA16154, R01CA154915, P41EB013598.

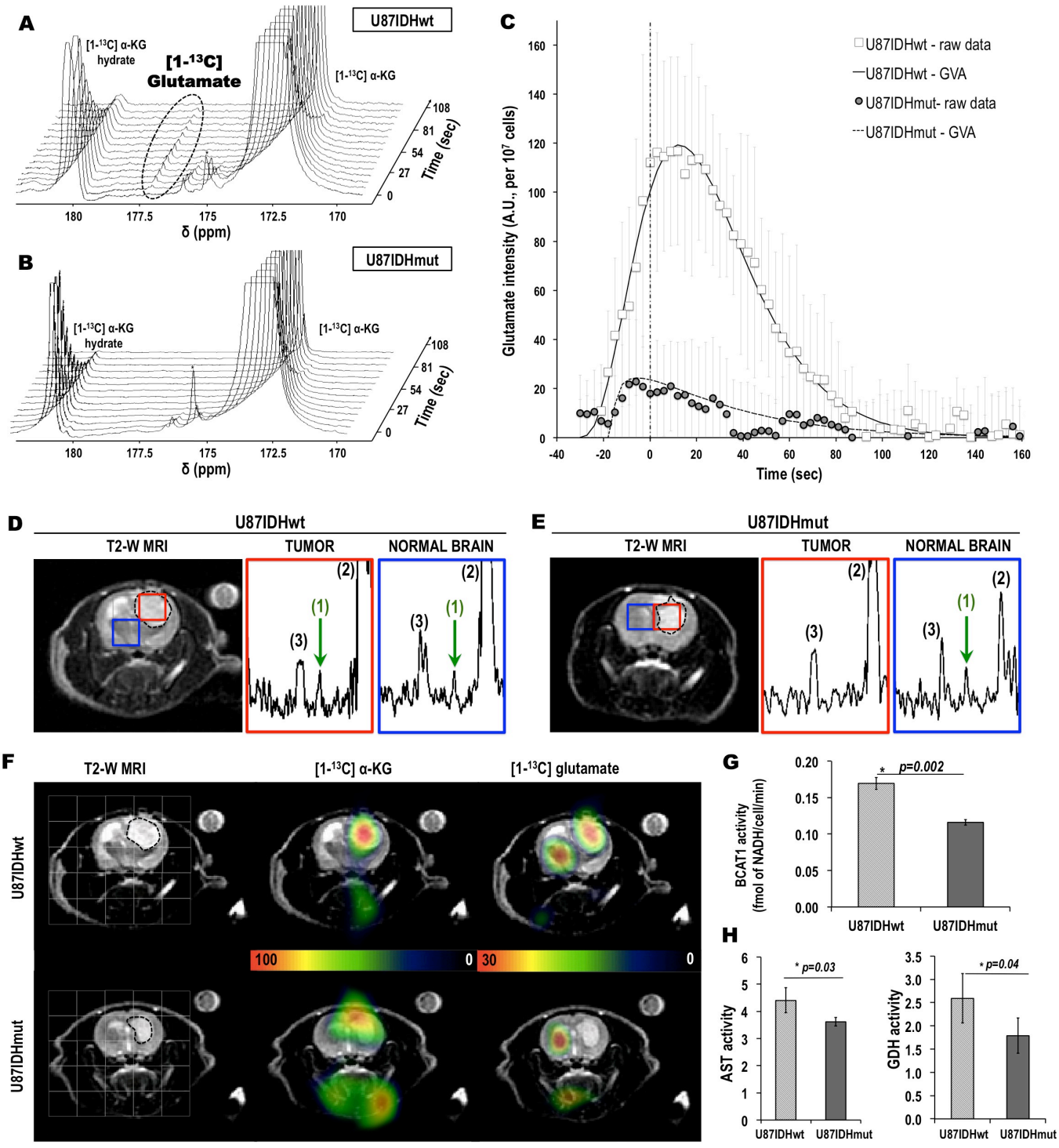

Figure Legend – Stack plots of dynamic ^{13}C MR spectra acquired at 11.7 Tesla following injection of HP α-KG in live **(A)** U87IDHwt and **(B)** U87IDHmut perfused cells (temporal resolution 9 seconds), showing the formation of HP glutamate in U87IDHwt cells only. **(C)** Intensities of HP glutamate in U87IDHwt (□) and U87IDHmut (**O**) perfused cells, showing the significantly higher level of glutamate in U87IDHwt cells as compared to U87IDHmut. The fit derived from the gamma-variate analysis (GVA) is displayed as a continuous line for U87IDHwt and as a dashed line for U87IDHmut perfused cells.T2-weighted MR images and corresponding hyperpolarized ^{13}C MR spectra of a **(D)** U87IDHwt and a **(E)** U87IDHmut tumor-bearing animals overlaid with tumor (red) and normal brain (blue) voxels from the 2D CSI acquisition. The observed resonances are: (1) HP glutamate (green arrow, δ_{GLU}=177.5ppm); (2) HP ($\delta_{\alpha\text{-}KG}$=172.6ppm); (3) HP α-KG hydrate ($\delta_{\alpha\text{-}KG\text{-}Hyd}$=180.9ppm). **(F)** T2-weighted MR images (first column) of a U87IDHwt (top) and a U87IDHmut (bottom) tumor-bearing animal overlaid with the grid used for 2D ^{13}C CSI acquisition. Corresponding heatmaps of HP α-KG and HP glutamate acquired 25 seconds post injection of HP α-KG. **(G)** BCAT1 enzymatic activity, **(H)** AST activity and GDH activity as measured by a spectrophotometric assays, are significantly decreased in mutant IDH1 cells as compared to wild-type cells (n=4 per cell line).

Design of an energy-independent SPECT gamma camera using a CZT detector and pixel-matched collimator

Srijeeta Bagchi, Fenghua Weng, Qiu Huang, Youngho Seo

Presenting Author
Name: Srijeeta Bagchi
Email: srijeeta.bagchi@ucsf.edu
Presenting Author's RIG/SRG: Nuclear Medicine
Presenting Author's Lab Location: China Basin

Senior Author
Name: Youngho Seo
Email: youngho.seo@ucsf.edu

Abstract highlights: SPECT suffers from limited detection efficiency and poor spatial resolution due to the need for collimators and indirect conversion of scintillation detectors. The main thrust of our study is to study the impact of collimator geometry and detector material on the performance of the front-end system using Monte Carlo simulations.

Introduction: SPECT suffers limited efficiency due to the need for collimators. Collimator properties largely decide the data statistics and image quality. The main thrust of our study is to evaluate the design of pixel-matched collimators to investigate their potential performances using Geant4 Monte Carlo simulations. Here, a pixel-matched collimator is defined as a collimator that is divided into the same number of pixels as the detector and the center of each pixel in the collimator is a one-to-one correspondence to that in the detector. The detector is made of Cadmium Zinc Telluride (CZT), which is one of the most promising materials for applications to detect hard X-rays and gamma rays due to its ability to obtain good energy resolution and high light output at room temperature. For our current project, we have designed a large-area, CZT- based gamma camera (20.48 cm × 20.48 cm) with a small pixel pitch (1.6 mm). The detector is pixelated and hence the intrinsic resolution can be as small as the size of the pixel. Materials of collimator, collimator hole geometry, detection efficiency, and spatial resolution of the CZT detector combined with the pixel-matched collimator were calculated and analyzed under different conditions. From the simulation studies, we found that such a camera using rectangular holes has promising imaging characteristics in terms of spatial resolution, detection efficiency, and energy resolution.

Methods: The proposed imaging system targets small volume imaging applications (potentially, breast, brain and prostate) to realize energy-independent SPECT, making it unnecessary to change collimators for different photon energies. Simultaneous multi-isotope imaging allows the exploration of various molecular and physiological functions under identical conditions. We show dual-isotope brain imaging using Tc-99m and I-123 for perfusion and striatal scans respectively. The projection data obtained from Geant4 simulation toolkit are used in an iterative reconstruction algorithm with attenuation correction to obtain reconstructed images.

Results: The results of simulated studies for sensitivity, spatial resolution, scatter, penetration, uniformity and energy spectra, and crosstalk in various settings of design parameters are shown to test and verify the potential performances of such a collimator-detector system. Simulations using digital phantoms such as flood and Hoffman phantoms show better sensitivity with resolution comparable to commercial collimators.

Conclusion: Numerical simulations to evaluate the design of a CZT-based detector combined with a tungsten-based pixel-matched collimator have been carried out. The results showed that such a camera with a pixel-matched collimator had a higher intrinsic resolution due to the small pixels and thus a better spatial resolution. The detection efficiency of the CZT has been compared with conventional ones using Monte Carlo simulations. The tungsten-based collimator has been shown to give a lower penetration rate than a lead-based one. At the same time, the energy resolution is improved by using CZT instead of NaI crystal. Furthermore, these results have indicated that the large CZT detector combined with a tungsten-based pixel-matched collimator is a promising gamma camera technology for an energy-independent SPECT system.

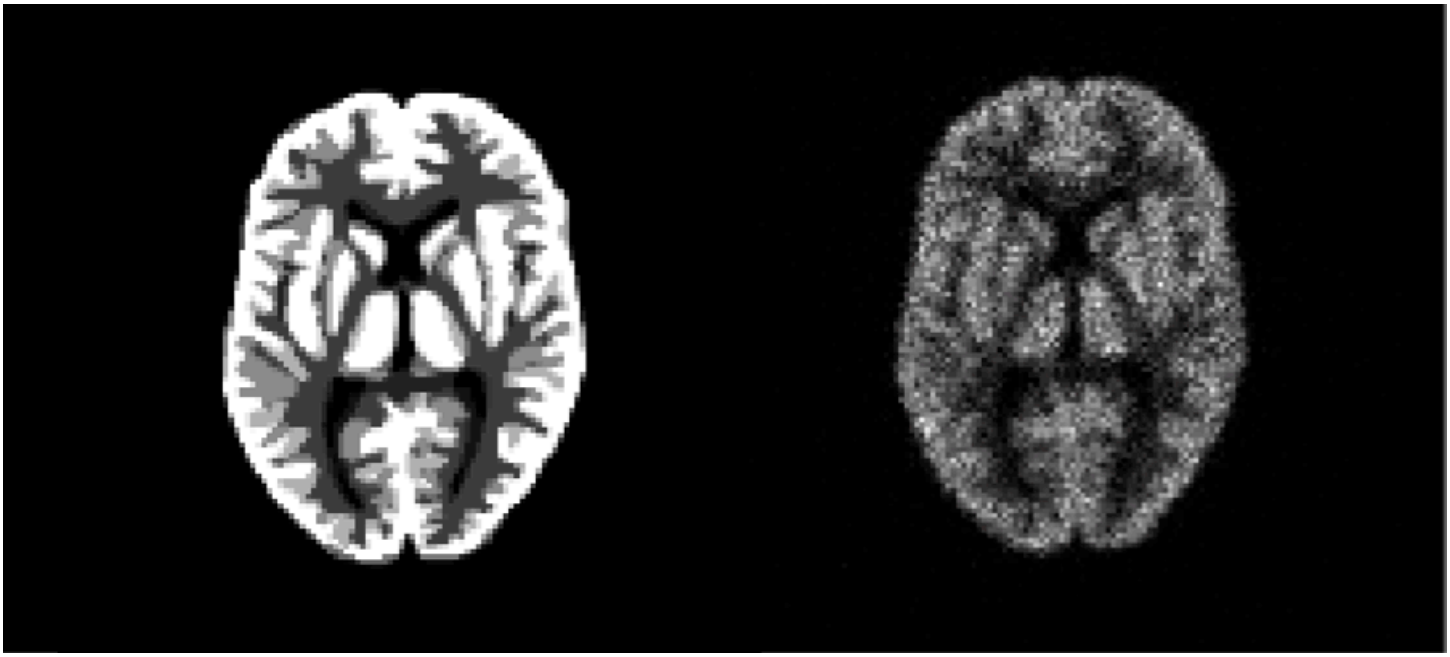

H2O2- labile [18F]FLT prodrug for sensing ROS in UOK262 renal carcinoma cells

Valerie Carroll, Brian W. Michel, Joseph Blecha, Henry VanBrocklin, Melanie Regan, Justin Delos Santos, Kayvan R. Keshari, Christopher J. Chang, David M. Wilson

Presenting Author
Name: Valerie Carroll
Email: valerie.carroll@ucsf.edu
Presenting Author's RIG/SRG: Nuclear Medicine
Presenting Author's Lab Location: China Basin

Senior Author
Name: David Wilson
Email: David.M.Wilson@ucsf.edu

Abstract highlights: A new peroxide sensitive prodrug, PC-[18F]FLT-1 has been synthesized for Imaging ROS in vivo using positron emission tomography (PET). Initial in vitro studies with UOK262 renal carcinoma cells indicate that the probe is capable of detecting small changes in added peroxide concentration as well as stimulated endogenous production of ROS.

Introduction: Reactive oxygen species (ROS) have been shown to play an important role in the development and progression of cancer and other diseases, yet imaging tools for sensing ROS in vivo are limited. The aim of this project is to develop a PET probe capable of sensing hydrogen peroxide in tumor microenvironments. Toward this goal, a new molecule peroxy-caged-[18F]fluorodeoxy thymidine (PC-FLT-1) has been synthesized. PC-FLT-1 reacts rapidly with H2O2 to generate [18F]FLT, allowing its peroxide dependent uptake and retention in proliferating cells.

Methods: [18F]FLT was prepared according to previously reported techniques. PC-[18F]FLT-1 was obtained by coupling [18F]FLT to a peroxide-labile aryl boronate. The peroxide dependent kinetics of FLT generation from PC-FLT-1 were monitored by HPLC. The relative uptake of PC-FLT-1 was investigated using H2O2-treated UOK262 renal carcinoma cells and a paraquat induced oxidative stress cell model. Blocking experiments were performed with co-administration of non-radioactive thymidine.

Results: In the presence of peroxide FLT is rapidly generated from PC-FLT-1 with a pseudo first order rate constant of 6.7 × 10-7 ± 0.4 × 10-7 s-1. PC-[18F]FLT-1 was obtained in a 41 ± 14% (n = 5) radiochemical yield from [18F]FLT. In vitro cell assays with PC-[18F]FLT-1 demonstrate a significant increase in signal from 0.4 ± 0.07% cell associated activity at 0 μM H2O2 to 1.22 ± 0.2% cell associated activity at 100 μM H2O2 at 1 h ($p = 0.0003$) and in the presence of paraquat ($p < 0.009$) at 4h.

Conclusion:
These results suggest that PC-FLT-1 exhibits promising characteristics for imaging of oxidative stress in vivo. Fu
extended to the in vivo study of other relevant analytes.

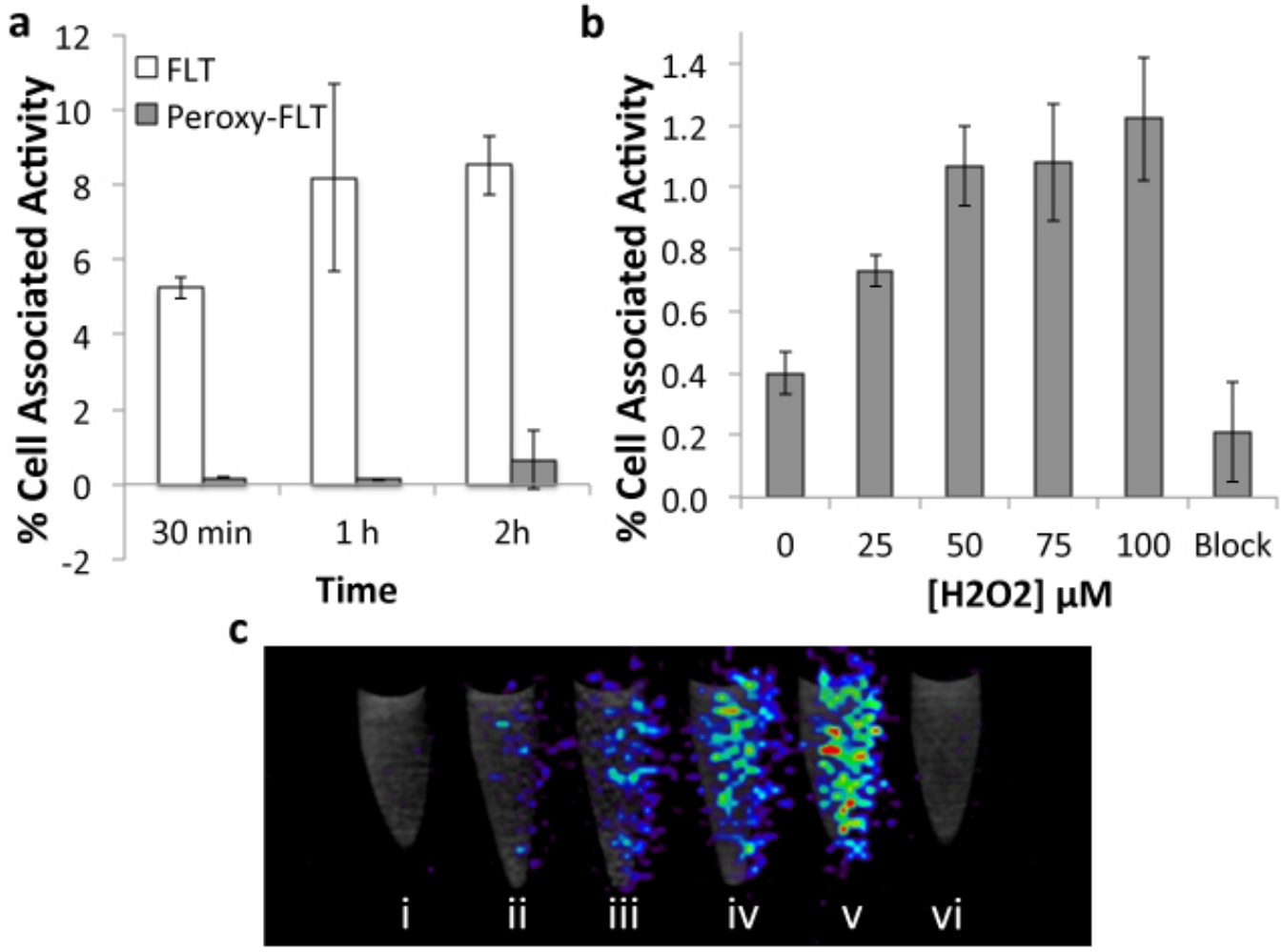

Figure 1. a) Cellular uptake of [^{18}F] in UOK262 renal carcinoma cells under normal conditions (-) H_2O_2. b) Peroxide dependent, (+) H_2O_2 [^{18}F] cellular uptake and thymidine (1 mM) blocking after 1h incubation. c) Phantom image of [^{18}F] cell uptake in the presence of i. 0 µM, ii. 25 µM, iii. 50 µM, v. 75 µM, iv. 100 µM H_2O_2 and vi. 100 µM H_2O_2 + 1 mM thymidine (block).

Biological Response to Bevacizumab Using FMISO PET/MR Imaging In Recurrent Glioma

Ramon F. Barajas Jr., Miguel H. Pampaloni, Soonmee Cha

Presenting Author
Name: Ramon Barajas Jr
Email: ramon.barajas@ucsf.edu
Presenting Author's RIG/SRG: Neuroradiology Nuclear Medicine
Presenting Author's Lab Location: Parnassus

Senior Author
Name: Soonmee Cha
Email: soonmee.cha@ucsf.edu

Abstract highlights: We provide initial FMISO PET/MR imaging of a patient with recurrent anaplastic astrocytoma following bevacizumab therapy. Combined imaging demonstrated decreased tumor hypoxia and enhancement. This observation suggests FMISO PET/MRI captures dynamic changes in the status of tumor hypoxia following the initiation of angiogenesis inhibitor therapy.

Introduction: Hypoxia is a potent stimulator of VEGF mediated angiogenesis, a requisite for tumor growth. Bevacizumab is a recombinant humanized monocolonal antibody against VEGF. Unfortunately, the ability to predict clinical outcome in patients with recurrent glioma undergoing bevacizumab therapy remains elusive. One noninvasive means of quantifying tissue hypoxia is through the use of FMISO PET imaging. A paucity of evidence regarding the role of hypoxic tumor burden in response outcome following bevacizumab therapy currently exists. Given the complex and synergistic interplay between hypoxia and angiogenesis, the quantification of hypoxic tumor burden may be useful in risk stratification of patients undergoing bevacizumab therapy. Therefore, the primary aim of this study is to investigate if changes in recurrent high grade glioma hypoxic burden, as assessed by contrast enhanced FMISO PET/MRI, occur concurrent with bevacizumab therapy.

Methods: A 65-year-old man with recurrent left temporal lobe anaplastic astrocytoma referred to our institution's neurological oncology service for bevacizumab therapy (879 mg IV every two weeks) was prospectively enrolled, following informed written consent, into this HIPAA and IRB compliant study. One week prior to and following the fourth dose of bevacizumab therapy the patient underwent contrast enhanced FMSIO PET/MR imaging. Simultaneous imaging was performed on a 3T wide bore investigational GE scanner 90 minutes following FMISO administration (7 mCi intravenously). Forty minute PET emission imaging was performed with time of flight reconstruction. Attenuation correction was performed using MR imaging techniques. Physiologic FMSIO PET images were co-registered with contrast-enhanced T1, T2, and FLAIR images using GE PET/MR review v1.0 allowing for the production of regions of interest (ROI). Semi-quantitative minimum (min), mean, and maximum (max) FMISO values were produced by standardization to ROI's placed on the right distal cervical internal carotid artery (tissue to blood; T/B value) and NAWM (rValue).

Results: Pre-bevacizumab FMSIO PET/MR imaging demonstrated locally recurrent contrast enhancing tumor about the left temporal resection cavity associated with elevated FMSIO uptake (T/B values, min 1.12, mean 1.43, max 1.65; rValues, min 1.72, mean 2.18, max 2.11). Follow-up FMSIO PET/MR examination occurring 10 weeks following the initial exam (8 weeks following first dose of bevacizumab therapy, 4 doses administered total) demonstrated a nonenhancing T2/FLAIR hyperintense mass about the posterior margin of the resection cavity that demonstrated reduced FMISO uptake (T/B values, min 0.46, mean 0.91, max 1.43; rValues, min 0.49, mean 0.71, max 1.65) (Figure 1).

Conclusion: Our initial experience suggests that FMSIO PET/MR imaging can noninvasively evaluate the biological effects induced by bevacizumab therapy in patients treated for recurrent high grade glioma. Specifically, hypoxic volume decreases concurrently with enhancing volume following angiogenesis inhibitor therapy. We continue to enroll patients in this study to further adjudicate the effects of bevacizumab therapy on tumor hypoxia burden.

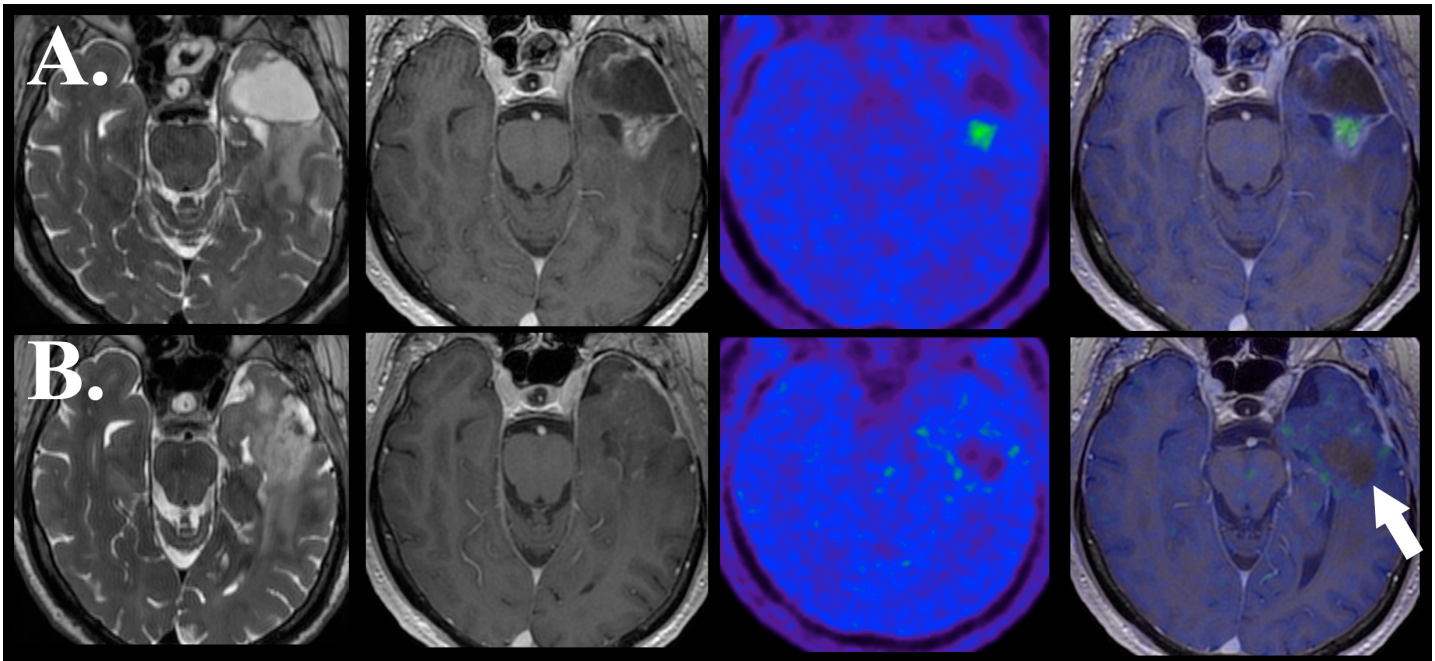

Figure 1: Single modality FMSIO PET/MR imaging of the brain in a patient with high grade glioma prior to (A) and 8 weeks following (B) bevacizumab therapy. Axial T2 (left), T1 post gad (center left), FMISO (center right), and fused FMISO T1 post gad (right) images demonstrate focal FMISO uptake within the contrast enhancing region on baseline imaging (Row A). Follow-up FMISO PET/MR examination demonstrates enlarged nonenhancing mass with reduced FMISO uptake compared to baseline imaging (Row B, arrow).

Selective Deletion of Nociceptors by Ganglionic Injection of Resiniferatoxin

Jacob Brown, Maythem Saeed, Michael Iadarola, Alan Basbaum, Loi Do, Mark Wilson, Steve Hetts, Bill Dillon

Presenting Author
Name: Jacob Brown
Email: jacob.brown@ucsf.edu
Presenting Author's RIG/SRG: Neuroradiology Neuro Interventional
Presenting Author's Lab Location: China Basin

Senior Author
Name: Bill Dillon
Email: William.Dillon@ucsf.edu

Abstract highlights: Resiniferatoxin (RTX) is a potent capsaicin receptor (TRPV1) agonist known to selectively delete pain transmitting neurons in small animals. This project leverages this mechanism by introducing CT-guided injection of RTX directly at the site of peripheral pain transmission in pigs for a highly localized treatment effect.

Introduction: The discovery of enriched expression of the vanilloid receptor (TRPV1) in nociceptive neurons of the dorsal root and trigeminal ganglia has been explored as a potential target for selective analgesia. Resiniferatoxin (RTX) is a TRPV1 agonist like capsaicin, only many times more potent, causing a large intracellular Ca2+ influx, which can be cytotoxic to cells. Importantly, TPRV1 is minimally expressed or absent in motor neurons and myelinated sensory pathways, allowing RTX to selectively delete pain transmitting neurons while leaving “bystander” neurons intact. Combining this molecular selectivity with the precision of CT guided delivery into peripheral pain generators has important potential to selectively treat severe pain.

Methods: Injections: RTX was delivered to dorsal root sensory ganglia along the lumbar spine using CT guidance in two farm pigs. Ganglia on one side of the animal were injected with either 500 or 2000 ng RTX + contrast. The contralateral side was injected with vehicle + contrast. Behavioral Analysis: Following treatment, a four week observation included lameness scoring, gate analysis and periodic stimulation with an infrared diode laser. Behavior was captured with video camera and time from laser stimulus to response was recorded during stimulating of both treated and untreated sensory dermatomes. Immunohistochemistry: Ganglia were dissected and numbers of TRPV1+ cells/HPF were compared.

Results: RTX can be precisely delivered to the dorsal root ganglia along the lumbar spine (L3, L4, L5, L6 levels) using CT guidance in farm pigs (see figure). Post injection delayed CT of the lumbar spine shows minimal diffusion of drug away from ganglia. Animals ambulate normally during 4 week observation as assessed by video recorded gate analysis and disability scoring (lameness score = 0). Withdrawal latency to laser stimulus is prolonged in sensory dermatomes innervated by treated ganglia (mean 9.9 sec, +/- 3.9) vs untreated (mean 5.7 sec +/- 1.1 sec). Immunohistochemistry confirms targeted effect of RTX on sensory ganglia as assessed by TRPV1+ cells per high power field.

Conclusion: With this pilot study we have validated that widely available CT technology can be used to precisely deliver the novel therapeutic RTX directly to sensory ganglia in a higher order mammal. Previous work demonstrates that RTX acts specifically on the TRPV1 receptor which is limited to pain transmitting neurons. Consistent with this, we observe a significant latency in animal response to nociceptive stimulation in treated sensory dermatomes compared with untreated areas, providing behavioral evidence that some pain transmitting neurons have been deleted. In contrast, we do not see any “bystander effect” on motor or other sensory neurons as treated pigs have normal gate and no observable motor deficits. In addition, numbers of TRPV1+ cells in sensory ganglia and spinal cord provide evidence of this effect at the cellular level. These early results introduce the principle that image guided delivery of RTX can precisely target a site of peripheral pain generation suggesting a new capability in personalized and selective pain medicine.

CT guided RTX injection localized to DRG at L6 in pig

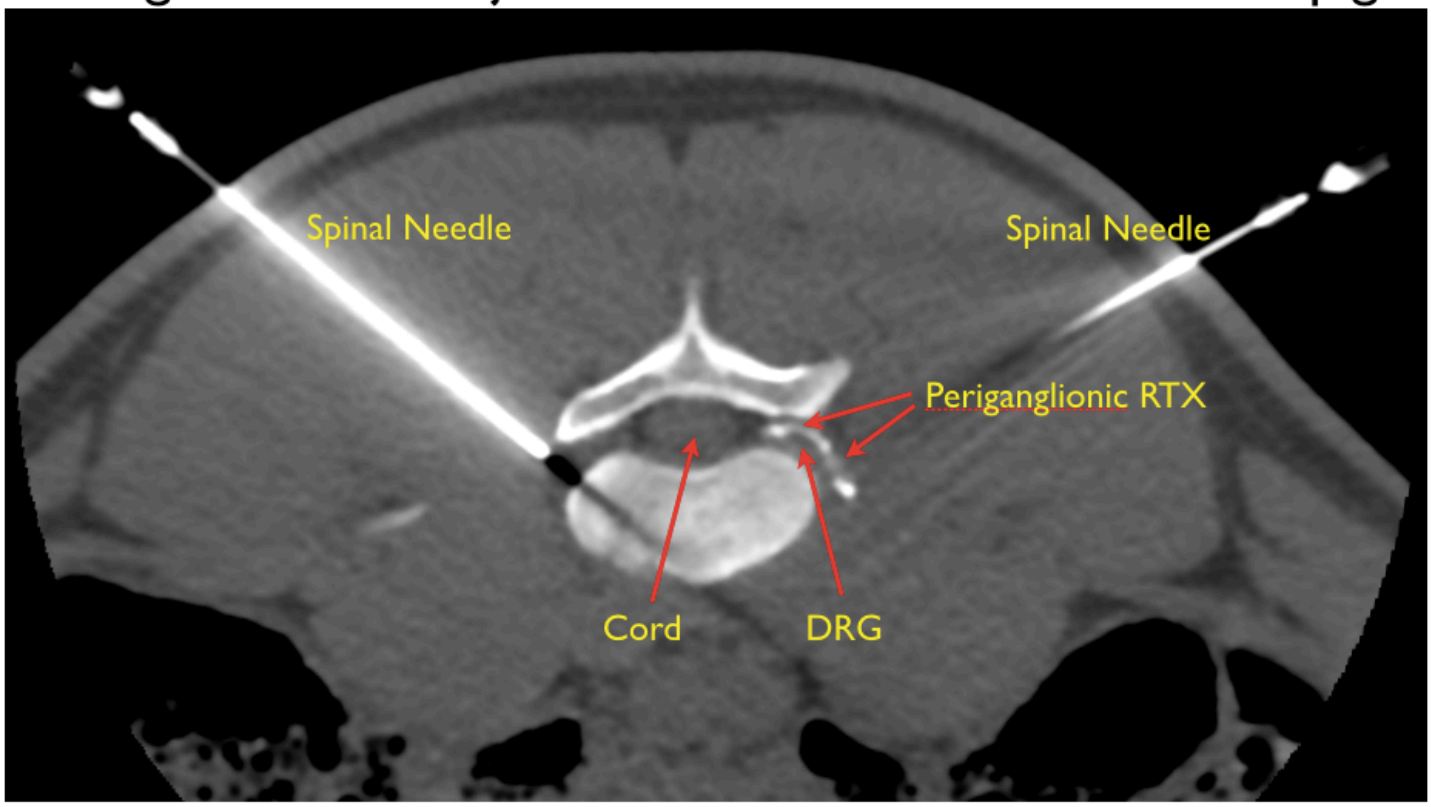

Anatomic Embedding of the Structural Connectome Within the Human Brain

Julia Owen, YiShin Chang, Pratik Mukherjee

Presenting Author
Name: Julia Owen
Email: julia.owen@ucsf.edu
Presenting Author's RIG/SRG: Neuroradiology
Presenting Author's Lab Location: China Basin

Senior Author
Name: Pratik Mukherjee
Email: pratik.mukherjee@ucsf.edu

Abstract highlights: We investigate the embedding of the structural connectome in the white matter of the human brain to uncover the relative importance of various white matter tracts to the network architecture of the brain.

Introduction: The structural connectome is a powerful construct that can be used to characterize the network structure of both the healthy and diseased brain. . The edges of the connectome traverse white matter to connect cortical and subcortical nodes, although the anatomic embedding of these edges is generally overlooked in the literature. Characterization of the embedded structural connectome could provide improved understanding of the relative importance of various white matter tracts to the network architecture of the brain. In addition, studying the embedding could serve as a tool to study white matter diseases with complex patterns of disconnection, where degradation may not solely obey the boundaries of white matter tracts, but instead sets of edges, utilizing only a portion of a tract or multiple tracts, may be affected.

Methods: In this work, we introduce edge density imaging (EDI), a post-processing technique for diffusion-weighted MRI data, which examines the embedding of the structural connectome by creating a map that represents the number of edges that pass through every white matter voxel. We use the diffusion-weighted MRI images acquired on a Siemens 3T TIM Trio MR scanner from 10 healthy control subjects (each scanned twice). Using tractography between gray matter regions defined by FreeSurfer, we can build up the path that each edge of the connectome takes through the white matter. Adding these binarized tractography results between every pair of regions yields an edge density image for a particular subject. The ED map for each individual was registered to the MNI brain template in order to create an average across subjects.

Results: Our results demonstrate spatially ordered variations of edge density (ED) throughout the white matter, including a strong posterior ED bias. Using test-retest data, we establish excellent to good reliability for our edge density calculations, and show consistent results using different cortical and subcortical parcellation schemes and scan acquisition parameters. We also demonstrate that ED yields complementary information to other previously described white matter voxel-wise parameters, including fractional anisotropy, track density, fiber orientation dispersion and neurite density. We map the white matter regions that are enriched with pathways connecting rich club nodes and also those with high densities of intra-modular and inter-modular edges, discovering that edges of the rich club and modules are not evenly distributed across the white matter. Specifically, we found that regions in the right superior parietal and left superior temporal white matter have greater number of rich club edges than complimentary, contralateral regions. Using edge betweenness centrality, we are able to identify regions involved in a large number of shortest paths, some of which are highly connected and others which are relatively isolated.

Conclusion: Taken as a whole, our analyses reveal an intricate relationship between white matter and connectome edges and motivate the use of EDI to study disorders of white matter to better understand how connectome edges navigate white matter in a diseased state.

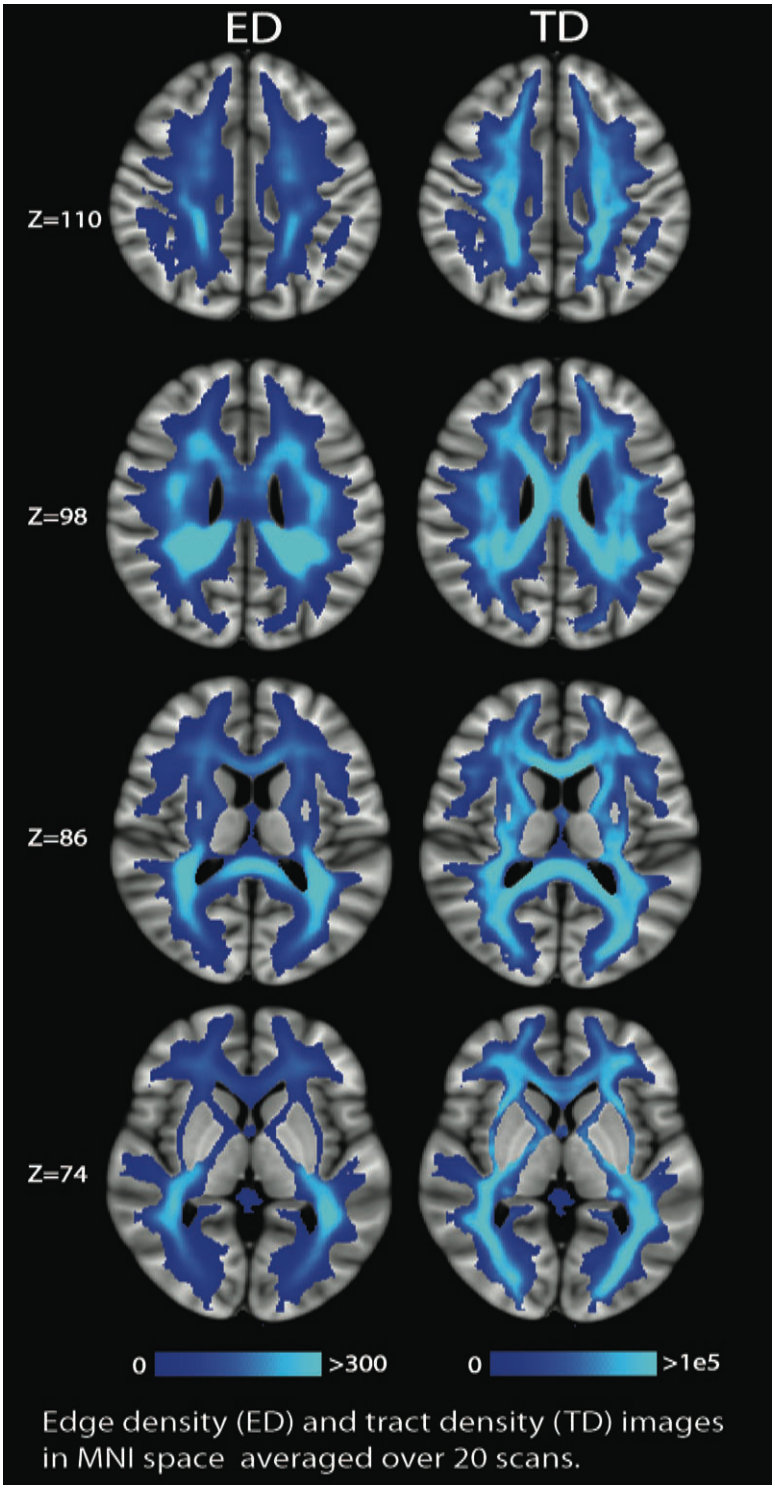

Edge density (ED) and tract density (TD) images in MNI space averaged over 20 scans.

Regional functional connectivity predicts distinct cognitive impairments in Alzheimer's spectrum

Kamalini G. Ranasinghe, Leighton B. Hinkley, Alexander J. Beagle, Danielle Mizuiri, Anne F. Dowling, Susanne M. Honma, Mariel M. Finucane, Carole Scherling, Bruce L. Miller, Srikantan S. Nagarajan, Keith A. Vossel

Presenting Author
Name: Kamalini Ranasinghe
Email: kranasinghe@memory.ucsf.edu
Presenting Author's RIG/SRG: Neurodegenerative Diseases
Presenting Author's Lab Location: Mission Bay

Senior Author
Name: Keith Vossel
Email: KVossel@memory.ucsf.edu

Abstract highlights: 1.Magnetoencephalographic imaging (MEGI) measures brain functional connectivity. 2.We investigated MEGI alpha-band connectivity in a cohort with Alzheimer's spectrum. 3.Decreased connectivity of focal brain regions correlates with cognitive deficits. 4.MEGI is a novel, unbiased approach to map neural network defects in dementia.

Introduction: Neurodegenerative diseases target specific vulnerable neuronal networks. Disturbance in synchronous neural oscillations is a fundamental component of network dysfunction. The relationship between distinct cognitive impairments in Alzheimer's disease and functional connectivity of distinct brain regions, however, is largely unknown.The objective of the current study was to to explore the relationship between regional defects in resting state functional connectivity patterns and specific cognitive deficits in Alzheimer's disease spectrum.

Methods: We examined the resting-state functional connectivity of alpha-band activity in 27 patients with Alzheimer's disease spectrum—22 patients with Alzheimer's disease and 5 patients with mild cognitive impairment due to Alzheimer's disease—and 15 age-matched controls without cognitive deficits. The Alzheimer's disease group included 5 patients with logopenic variant primary progressive aphasia, 7 patients with posterior cortical atrophy, and 10 patients with early-onset amnestic/dysexecutive Alzheimer's disease. We used magnetoencephalographic imaging (MEGI) to perform an unbiased search for regions where patterns of functional connectivity correlated with cognitive performance on a battery of neuropsychological tests and with disease severity. Functional connectivity measured the strength of coherence between a given region and the rest of the brain.

Results: We found that 1) decreased functional connectivity of the left frontal cortex correlated with deficits in executive control and episodic memory, 2) reduced functional connectivity of the left inferior parietal cortex correlated with visuospatial impairments, and 3) reduced neural connectivity of multiple bilateral brain regions including the right temporo-parietal region and left middle frontal cortex correlated with higher degree of disease severity. In our disease cohort, MEGI-derived functional connectivity was a more sensitive indicator of cognitive dysfunction than MRI measures of grey matter volume, and brain atrophy did not account for the regional MEGI functional connectivity deficits.

Conclusion: Our findings indicate that reductions in region-specific alpha-band resting-state functional connectivity predict, and might contribute to, specific cognitive deficits in Alzheimer's disease. In future studies, MEGI functional connectivity could be an important biomarker to map and follow the progress of early cognitive deficits in Alzheimer's disease.

Variability of resting-state cortical functional connectivity in hypoxic-ischemic infants

Trevor Flynn, Srivathsa Veeraraghavan, Donna Ferriero, A James Barkovich, Duan Xu

Presenting Author
Name: Trevor Flynn
Email: trevor.flynn@ucsf.edu
Presenting Author's RIG/SRG: Pediatrics/Fetal
Presenting Author's Lab Location: Mission Bay

Senior Author
Name: Duan Xu
Email: duan.xu@ucsf.edu

Abstract highlights: Interindividual variability in resting-state functional connectivity was quantified in 96 cortical ROIs across a population of hypoxic-ischemic infants six months after birth. Connectivity in frontal and temporal regions exhibited significantly higher variability across our population, indicating that these areas may serve as indicators for clinical outcome.

Introduction: Functional connectivity in the human brain has been intensely studied in order to delineate the underlying framework of human cognition and behavior. Individual differences in resting-state functional networks have been demonstrated to correlate with neurobehavioral variability, including differences in symptom severity for a variety of neuropsychiatric disorders. Quantifying the interindividual variability of resting-state functional connectivity in clinical populations could help us to both understand the neural underpinnings of a disorder and identify neurological markers that predict clinical severity or outcome. Here we employ two methods to characterize the variability of resting-state functional connectivity in hypoxic-ischemic infants six months after birth, with the goal of identifying high-variability anatomical regions for further study.

Methods: Diffusion and functional MRI scans were performed on 33 term-born infants with hypoxic-ischemic brain injury six months after birth. The infants were scanned on a 3T GE DISCOVERY MR750 scanner with T1 3D IRSPGR (256x256 matrix, TI=450, flip angle=15°) and resting state BOLD fMRI using gradient echo EPI (64x64 matrix, TR=2000, TE=20, 200 repetitions). Functional data was preprocessed by applying motion correction, 5mm spatial smoothing and a high-pass filter of 1/50 TRs (100s) to our BOLD data and regressing out CSF signal, then registering our BOLD data to the NIHPD Objective 1 Pediatric Atlas using each infant's corresponding T1 scans as an intermediate. The BOLD global mean time series and motion parameters were computed using FSL's GLM tool. Registered brains were parcellated into 96 cortical anatomical ROIs by registering the Harvard-Oxford Cortical Atlas parcellations to the pediatric template. For each ROI, both a seed voxel correlation map and inter-ROI correlation matrix were obtained and the inter-subject variability of these connectivity metrics for each ROI was determined by averaging all possible pairwise correlation coefficients between subjects.

Results: Figure 1 shows the distribution of anatomical regions of high and low interindividual variability of ROI seed voxel correlation maps across our study population. Overall, right hemisphere ROIs exhibited significantly higher mean variability than left hemisphere ROIs ($p=0.036$). Regions with significantly higher interindividual variability in seed voxel correlation maps included broad portions of the frontal cortex and temporal cortex (excluding the tempero-occipital inferior temporal gyrus) as well as the subcallosal cortex and the anterior division of parahippocampal gyrus. Areas of significantly lower interindividual variability in seed voxel correlation maps included the precentral and postcentral gyri, superior parietal lobe, lateral occipital cortex, intracalcarine cortex, precuneus, lingual gyrus, occipital fusiform gyrus, supracalcarine cortex as well as the tempero-occipital inferior temporal gyrus and posterior division of the parahippocampal gyrus. Inter-ROI mean time series correlation variance maps are a work in progress.

Conclusion: Our study has demonstrated interindividual variability of resting-state functional connectivity in hypoxic-ischemic infants to be nonuniform across the cortex, with frontal and temporal regions typically exhibiting high variability and parietal and occipital regions exhibiting low variability. Further investigation into the variation of anatomy and connectivity in these high-variability regions could yield useful predictors for outcome in our clinical population.

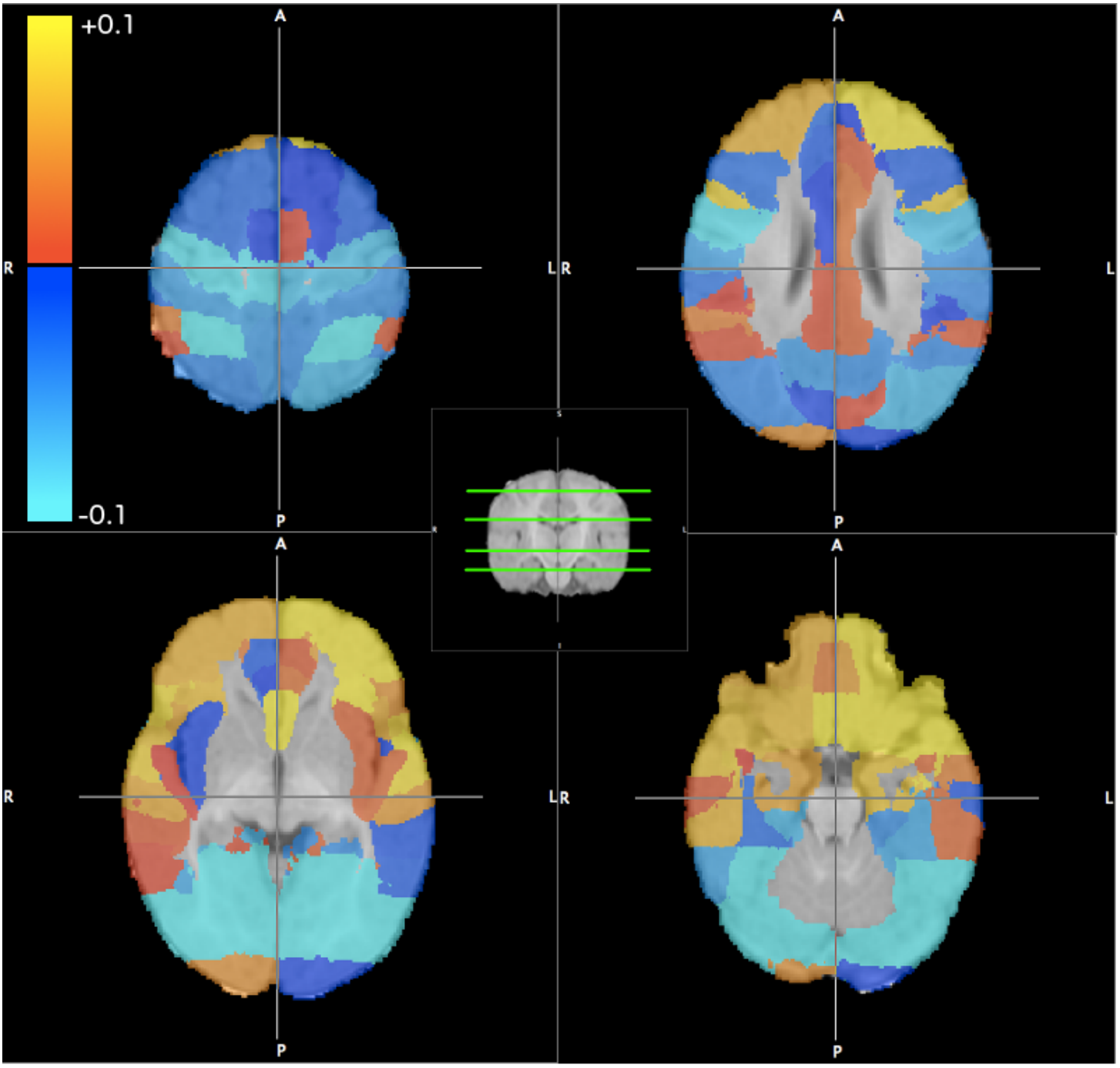

Figure 1. Relative variability of seed voxel correlation maps across study population. Positive (red-yellow) values indicate higher regions of higher variability than corresponding mean hemispheric variability.

MRI Quantification of Function, Perfusion and Viability in Microembolized Ischemic Myocardium

Loi Do, Skylar Nahi, Brenda Zheng, Mark Wilson, Maythem Saeed

Presenting Author
Name: Loi Do
Email: loi.do@ucsf.edu
Presenting Author's RIG/SRG: Cardiac & Pulmonary Imaging
Presenting Author's Lab Location: China Basin

Senior Author
Name: Maythem Saeed
Email: maythem.saeed@ucsf.edu

Abstract highlights: MRI detected the structural and functional changes in moderately ischemic myocardium with and without microemboli. MRI has potential for monitoring infarct resorption but has limited spatial resolution for detecting microinfarcts. Cine, perfusion and DE-MRI can be used to test efficacy of cardioprotective therapies designed to improve LV function and healing.

Introduction: Large variation in volume/size of dislodged microemboli during spontaneous or percutaneous coronary intervention (PCI), myocardial infarction (MI) size, imaging time after revascularization and lack of biopsy, makes it challenging to study microemboli effects in clinical settings. Therefore, defined parameters are necessary for noninvasive evaluation. The purpose of this study was to 1) provide detailed analysis and comparison of infarct healing in ischemic myocardium with and without microemboli and 2) validate MRI measurements against histochemical/histopathological staining.

Methods: PCI was performed under fluoroscopy in 16 pigs. Additionally 8 pigs served as controls (Group I). The left anterior descending coronary artery (LAD) was occluded for 45min (group II, III) by a balloon catheter and in group III, microemboli (32mm3 volume, 40-120μm diameter) were delivered in the LAD prior to reperfusion. A 1.5T MR scanner was used at 3 days and 5 weeks to acquire ECG-gated cine MRI in all groups and perfusion and delayed contrast enhanced MRI (DE-MRI) in groups II and III followed by euthanasia. The hearts were excised and sliced and each LV ring was then incubated in TTC (triphenyltetrazolium chloride) to delineate microinfarct. Tissues were fixed by 10% formalin then stained with Masson trichrome to measure scar tissue. Infarct size on DE-MRI, TTC and histology were then compared.

Results: Both intervention groups showed significantly greater deleterious effects on structural and functional cine, perfusion and DE-MRI indices than controls. Increase in LV end systolic volume and decrease in ejection fraction were more pronounced in group III than II or controls. Group III (8/8 and 8/8) demonstrated regional perfusion deficits at 3 days and 5 weeks compared with group II (5/8 and 3/8 respectively), reflected by max upslope, time to max signal intensity and max signal intensity. Large MI and patchy microinfarct at the border zone was also visible in group III on DE-MRI. TTC revealed similar findings to DE-MRI in both groups. At 3 days the extents of infarction were 3.3±2.2(g) in group II and 9.8±0.6 and in group III, and at 5 weeks1.3±0.9(g) and 7.7±0.5, respectively. Substantial reduction (60%) in infarct extents were documented in group II, but was significantly less (22%, $P<0.05$) in group III, suggesting delayed infarct healing. Traces of inflammatory cells/erythrocytes were visible in group III at 5 weeks (Fig). Histochemical TTC confirmed the infarct size on MRI (1.6±1.0(g) and 9.2±1.6). Infarct extents were greater on microscopy in group II (2.8±0.4) and III (13.4±2.4) than both MRI and TTC as well as LV mass 110±2 ($P=0.02$) in group III, 99±4 in group II and 93±4 in group I.

Conclusion: MRI detected the structural and functional changes in moderately ischemic myocardium with and without mechanical microvascular obstruction. In remote myocardium moderate compensatory hypertrophy was observed in ischemic microembolized myocardium compared with only ischemic myocardium. DE-MRI has the potential to monitor infarct resorption but has limited spatial resolution for detecting microinfarcts. MRI can be used to test the efficacy of cardioprotective therapies and distal protective devices in improving LV function and healing.

FID navigator for motion compensation in 3D black blood carotid MRI

Henrik Haraldsson, Sinyeob Ahn, Chengcheng Zhu, David Saloner

Presenting Author
Name: Henrik Haraldsson
Email: Henrik.Haraldsson@ucsf.edu
Presenting Author's RIG/SRG: Cardiac & Pulmonary Imaging
Presenting Author's Lab Location: VAMC

Senior Author
Name: David Saloner
Email: David.Saloner@ucsf.edu

Abstract highlights: A new FID navigator is proposed to reduce motion artifacts in 3D black blood carotid imaging. For evaluative purpose, subjects were instructed to swallow every 20 second during data acquisition. The FID navigator detected the motion, and reduced the image artifacts compared to data acquired without the FID navigator.

Introduction: Multi-contrast weighted MR imaging of the atherosclerotic carotid artery has been shown to be important in characterizing high risk plaque. However, this characterization may be hampered by motion artifacts. A recent multi-center study reported that approximately 15% of patient data cannot be used for clinical diagnosis due to motion contamination. An FID navigator has previously been utilized and evaluated for the reduction of motion artifacts in 2D turbo spin echo (TSE) imaging. The purpose of this study is to evaluate the feasibility of a new FID navigator for reducing motion artifacts in 3D black blood carotid imaging.

Methods: Data from four healthy volunteers was obtained on a 3T Skyra system (Siemens Medical Solutions) using the 3D spoiled gradient echo (FLASH) sequence (resolution: 0.8 mm isotropic, scan time: 3:15 min) in a coronal slice orientation with a Delay Alternating with Nutation for Tailored Excitation (DANTE) preparation pulse train to suppress the signal of the blood. DANTE pulses attenuate signal from moving spins significantly while minimally affecting stationary spins. A new FID navigator was introduced and combined with the sequence in which a statistical model was used to determine the acceptance/rejection of an acquired signal and consequent reacquisition at the end when being rejected. For simulation purpose, subjects were instructed to swallow every 20 seconds by visual cue signal. To evaluate motion and the reduction of motion artifacts with the proposed technique, three separate scans were run. (1) monitoring mode: all signals were accepted and acquired while FID signal was recording motion (2) gating mode: signals were accepted/rejected-reacquired by the decision of FID navigator and (3) data were acquired while subjects were instructed to remain still and this dataset served as a reference to the other two. All three datasets was reformatted transversally for illustrative purpose.

Results: The monitored acquisition showed that compared to the non-motion condition (top row in figure), the swallowing motion introduced artifacts in the form of: blurring (second row, volunteer 1 and 3), signal loss in the vessel wall (second row, volunteer 2), and ghosting (second row, volunteer 4). The third row illustrates that the proposed method using the new FID-gated acquisition reduces these artifacts. The FID navigator was applied for all sequences (reference, monitored, and gated) and a theoretical rejection rate was calculated. The rejection rate for the reference, monitored and gated sequence were 6%, 18%, and 21% for volunteer 1; 3%, 10%, 22% for volunteer 2, 5%,13%, and 15% for volunteer 3, and 6%, 15% and 16% for volunteer 4, respectively.

Conclusion: The new FID navigator applied to 3D FLASH sequence showed to reduce image artifacts caused by swallowing. The new FID navigator reduces the likelihood of failed studies and provides an easy-to-use reduction approach as it does not require detailed planning and positioning of the navigator, in contrast to traditional navigator-based approaches. 3D DANTE-FLASH was used in this study as it provided good image quality without flowing artefacts, therefore the swallowing motion can be evaluated stand-alone.

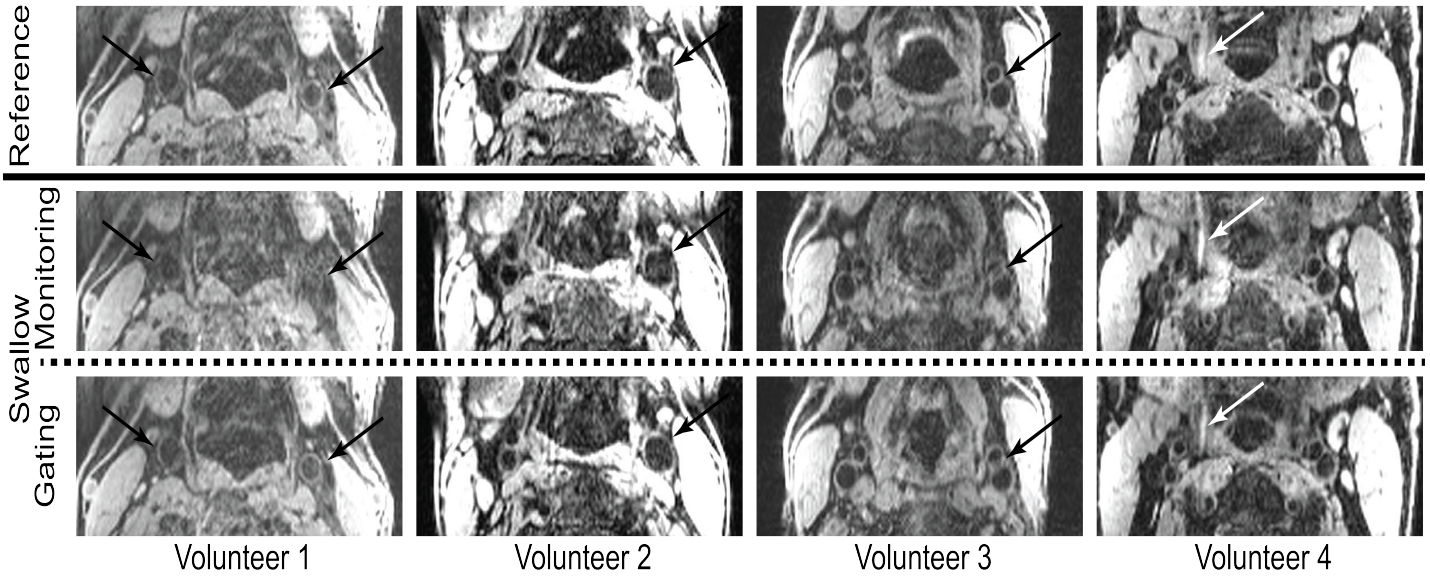
Reference
Swallow Monitoring
Swallow Gating
Volunteer 1
Volunteer 2
Volunteer 3
Volunteer 4

Ultrasound Findings in Failed Pancreas Transplants

Tara A. Morgan, Vickie A. Feldstein, Jack Harbell, Peter G. Stock, Rebecca Smith-Bindman

Presenting Author
Name: Tara Morgan
Email: Tara.Morgan@ucsf.edu
Presenting Author's RIG/SRG: Ultrasound
Presenting Author's Lab Location: Parnassus

Senior Author
Name: Rebecca Smith-Bindman
Email: Rebecca.Smith-Bindman@ucsf.edu

Abstract highlights: On ultrasound evaluation of pancreas transplants, abnormal spectral Doppler findings with absent or reversed end-diastolic arterial flow is strongly predictive of subsequent transplant failure; 55% of failed transplants had this abnormality identified, whereas only 7% of functioning transplants demonstrated this feature.

Introduction: Approximately 1000 pancreas transplants are performed annually in the US. They are susceptible to failure in the early post-operative period. Anticoagulation is often used as preventive therapy to minimize risk of splenic vein thrombus, which is associated with 1/2 of early transplant losses. UCSF is a large pancreas transplant center. Patients here undergo routine post-operative ultrasound (US) imaging. We sought to determine whether findings seen on Doppler US predict pancreas transplant failure.

Methods: Retrospective cohort study of pancreas transplants performed at UCSF between 01/2003 - 12/2012. All US examinations performed within the first post-operative year were reviewed. Allograft failure was assessed up to 1 year following transplantation. Transplant failure was defined as recurrent hyperglycemia/return to insulin dependence or following surgical pancreatectomy. 3 US features were assessed: presence of flow within the splenic vein; presence/character of arterial flow within the pancreas; and transplant edema. Thrombus involving >50% of the length of the splenic vein was deemed “splenic vein thrombosis.” Arterial flow within the allograft was defined as abnormal if, on spectral Doppler waveforms, there was absent or reversed diastolic flow. Edema was deemed present if AP diameter of the pancreas measured >3 cm.

Results: 257 pancreas transplants were performed. 211 transplants in 208 patients are included. Overall, 17 (8%) of the transplants failed and time until transplant failure ranged from 1-307 days. Reversed/absent end-diastolic flow on Doppler US was identified in 9 of 17 transplants that failed (sensitivity 53%, 95% CI 28%, 77%) and 13 of 194 transplants that did not fail (specificity 93%, 95% CI 89%, 96%), LR 7.9 (95% CI 4.0, 16). Splenic vein thrombosis was identified in a slightly higher number of failed transplants (n=10, sensitivity 59%, 95% CI 33%, 81%) but also was seen in more transplants that did not fail (n=22, specificity 89%, 95% CI 83%, 93%), LR 5.2 (95% CI 3.0, 9.1). Edema was noted in 10 failed transplants (sensitivity 59%, 95% CI 33%, 81%) but was seen much more frequently in transplants that did not fail (n=59, specificity 70%, 95% CI 63%, 76%), LR 1.9 (95% CI 1.2, 3.0). Each of the 3 US features was significantly associated with transplant failure when considered alone. However, when all 3 were included in the multivariate model, only absent/reversed end-diastolic arterial flow remained a significant predictor of transplant failure.

Conclusion: In this cohort of 211 pancreas transplants, abnormal arterial Doppler findings with absent/reversed end-diastolic flow was strongly predictive of transplant failure within 1 year; 55% of failed transplants had this abnormality identified, whereas only 7% of functioning transplants demonstrated this feature. Reversed end-diastolic arterial flow on spectral Doppler US of pancreas transplants is strongly predictive of subsequent failure. Although splenic vein thrombus and edema are often present in failed transplants, these observations are non-specific and not predictive of subsequent loss. Pancreas transplant US evaluations should include Doppler assessment of arterial flow and abnormal waveforms with absent end-diastolic flow should be considered a strong risk factor for transplant failure.

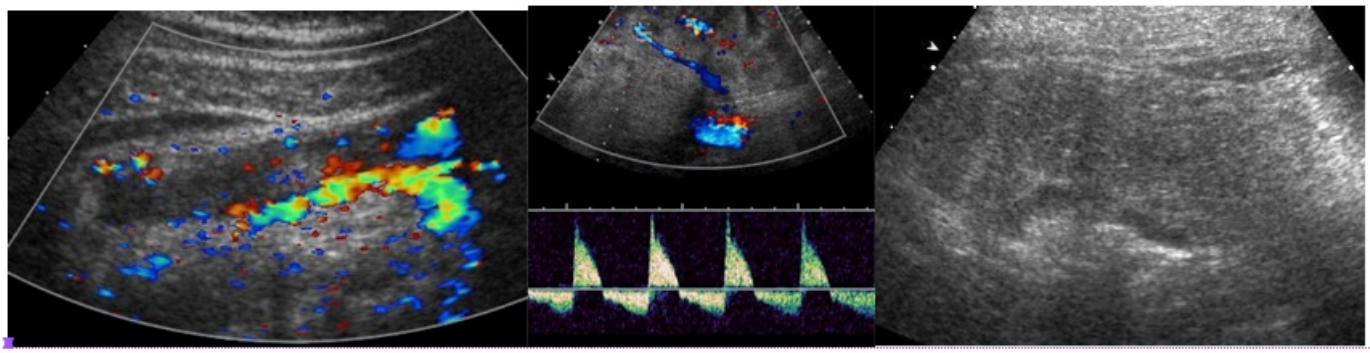

Development of Endovascular Chemotherapy Filter for Removing Doxorubicin from Blood: In Vivo Study

Jeffrey Yang, Chia-Hung Sze, Anand S. Patel, Maythem Saeed, Daniel L. Cooke, Albert K. Chin, Mark W. Wilson, Steven W. Hetts

Presenting Author
Name: Jeffrey Yang
Email: jeffrey.yang@ucsf.edu
Presenting Author's RIG/SRG: Interventional Radiology
Presenting Author's Lab Location: China Basin

Senior Author
Name: Steven Hetts
Email: steven.hetts@ucsf.edu

Abstract highlights: A novel prototype disposable endovascular chemotherapy filter (CF) device was developed to remove excess doxorubicin from the blood during intra-arterial chemotherapy delivery to prevent systemic toxicities. In this study, CF navigation, deployment and in vivo Dox binding was evaluated under x-ray fluoroscopy in the porcine inferior vena cava.

Introduction: Hepatocellular carcinoma (HCC) is the third leading cause of death worldwide and has faster growing mortality than many other cancers. Selective catheter-directed intra-arterial chemotherapy (IAC) is a standard treatment for unresectable HCC. Previous studies have shown that first-pass hepatic clearance of Doxorubicin (Dox) is between 50-70%. Moreover, Dox can cause bone marrow suppression, alopecia, gastrointestinal toxicity and heart failure at standard dose of 50-75 mg, and irreversible cardiac failure at cumulative doses above 360 mg. Therefore, the amount of Dox dose safely delivered during IAC is limited. Clinical and experimental studies demonstrate a positive linear relationship between Dox dose and tumor suppression, providing motivation for delivering high doses of Dox. Ion exchange resins demonstrated a high affinity to bind and eliminate Dox in vivo. Development of an intravascular catheter device containing ion-exchange resin that could eliminate Dox in the veins draining a transarterially-targeted organ, such as the liver, would encourage the use of higher Dox IAC dose while still limiting systemic toxicity. A novel prototype disposable endovascular chemotherapy filter (CF) device was developed to remove excess doxorubicin (Dox) from the blood during intra-arterial chemotherapy (IAC) delivery to prevent systemic toxicities. Previous proof-of-concept established the capacity of the filter to bind Dox in swine serum in vitro. In this study, CF navigation, deployment and in vivo Dox binding was evaluated in the porcine inferior vena cava (IVC).

Methods: An 18Fr CF device was constructed with an ion-exchange membrane attached to an expandable 28mm diameter Nitinol frame (Fig 1B). Under X-ray fluoroscopy and contrast venography, the CF was percutaneously introduced via the internal jugular vein and deployed in the porcine infrarenal IVC (Fig 1A). 50 mg of Dox was injected over 10 min in the IVC below the CF device. Venous catheters with tips proximal and distal to the CF device in the infrarenal IVC obtained pressures and blood samples for Dox concentrations over 90 min cross the CF device membrane.

Results: The CF device was successfully introduced and deployed in the infrarenal IVC in vivo. Visualization under X-ray fluoroscopy verified the proper placement and mechanical expansion of the Nitinol framework. In a 90 min study, the device was biocompatible, not leading to hemodynamic disturbances: pressure measurements taken throughout the experiment yielded a maximum gradient of 17 mmHg across the CF membrane. Venography demonstrated non-flow limiting thrombus associated with the CF device after 90 min of deployment (swine were not heparinized). Significant Dox binding was noted with an 85%, 74%, and 83% decrease in relative pre- versus post-filter Dox concentrations at times 3, 10, and 30 min, respectively after Dox injection (Fig 1C).

Conclusion: We developed a biocompatible CF device that can be safely introduced, deployed, and removed from the IVC in vivo. The CF device demonstrated significant Dox binding, and could serve as a platform technology in drug therapy to allow for higher regional doses of drug while limiting systemic toxicity. In future in vivo experiments, animals or the CF device itself will be heparinized in order to prevent thrombosis.

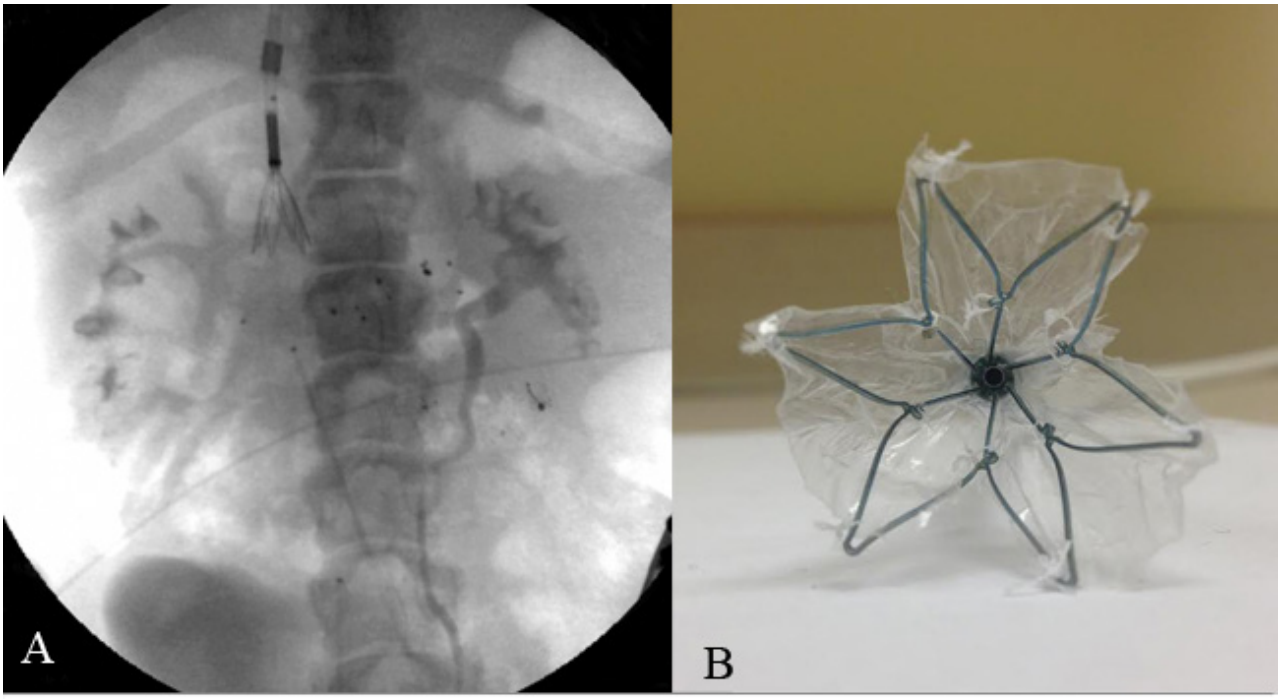

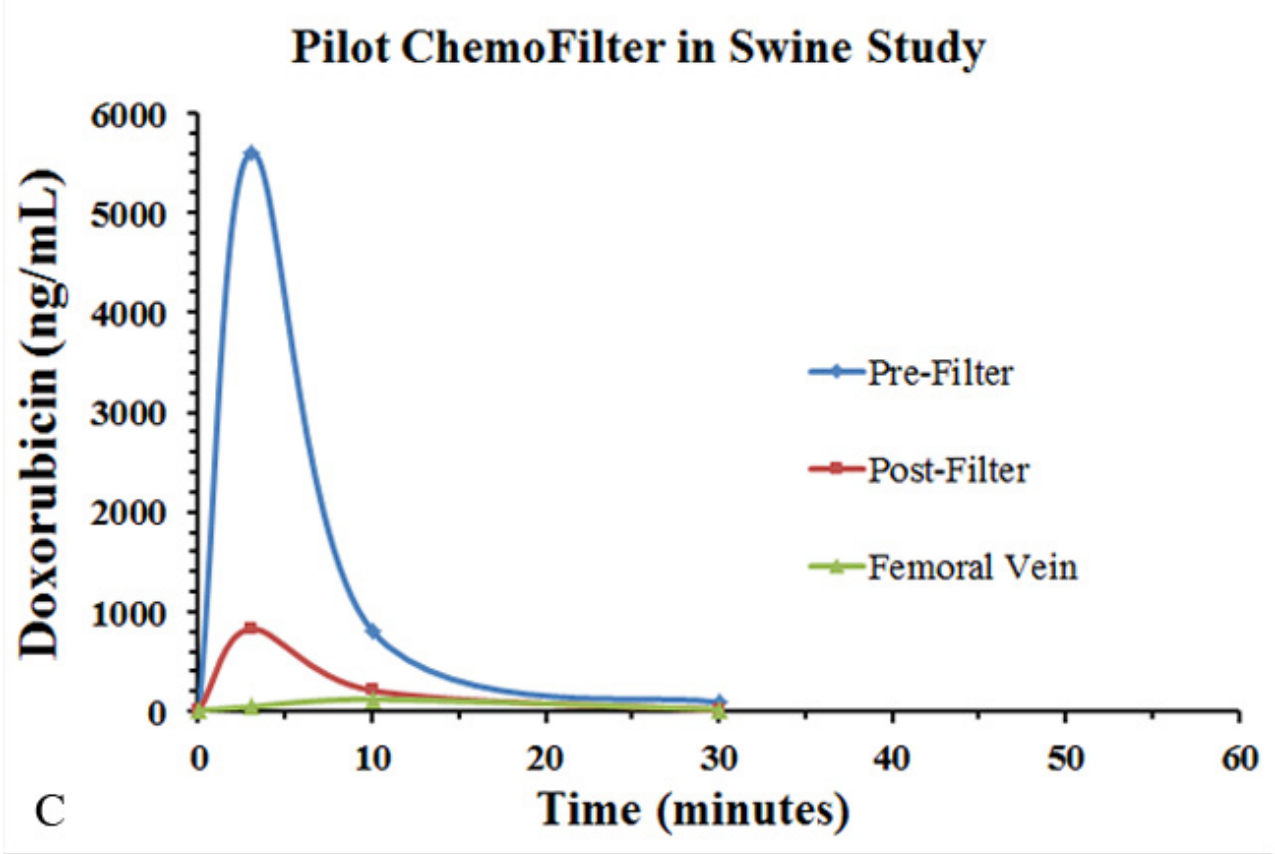

Figure 1. Catheter prototype with self-expanding nitinol tulip frame deployed in the IVC of a pig undergoing Dox infusion and filtration. (A) Fluoroscopic image of the swine demonstrating the ChemoFilter device in place with associated sampling catheters. (B) The expanded ChemoFilter device en-face. Notice nitinol cage with polymer resin membrane sutured onto the cage. (C) Dox concentration versus time with ChemoFilter in place during infusion of Dox in the infrarenal IVC. An 85% reduction in Dox concentration between pre-filter and post-filter samples at 3 minutes during peak infusion is consistent with Dox binding to the ChemoFilter.

Poster Presentations

#	Presenting Author	Abstract Title
1	Geetha Mohan	Effect of Kartogenin treatment in experimental osteoarthritis assessed using high-resolution MRI
2	Jesus Avila	Accurate body composition measures from simple whole body silhouettes
3	Aditi Guha	Longitudinal evaluation of Knee Osteoarthritis using Diffusion and Correlation with T1rho/T2 values
4	Martin Kretzschmar	Association of physical activity and knee abnormalities obtained from 3T MRI: Data from the OAI
5	Keiko Amano	Knee bone shape features correlate with abnormal tibial motion after ACL injury and reconstruction
6	Cory Wyatt	Baseline T1rho/T2 Correlate with Hip Cartilage Lesion Progression at 18 months
7	Bennett Ng	Statistical Appearance Modeling of Whole-Body Bone Shape and Density
8	Gabby Joseph	A reference database of cartilage T2 values in knees without cartilage degeneration
9	Favian Su	Feasibility of radiocarpal cartilage T1ρ MR imaging in rheumatoid arthritis
10	Prachi Pandit	T1p and T2-based characterization of IVDs for early detection/progression of degenerative changes
11	Chengcheng Zhu	3D isotropic black blood MRI of abdominal aorta vessel wall using DANTE-SPACE
12	Nichol Burris	Evaluation of Bicuspid Aortic Valve Fusion Pattern and Aortic Shape using 2D Phase Contrast MRI
13	Michelle Moghadassi	CT Radiation Dose in Patients with Suspected Nephrolithiasis
14	Liqin Zhao	Does addition of ASIR improve the dual energy CT monochromatic image quality in portal venography?
15	Cornelius von Morze	Imaging Fasting-Induced Modulation of Hepatic / Renal Lactate Metabolism by Hyperpolarized C-13 MRSI
16	Brittany Bartolome	Retrospective Review of Transjugular Liver Biopsy in Patients with Left Lobe Only Liver Transplants
17	Prasheel Lillaney	In Vivo Assessment of a Renal Artery Intervention using the MARC Catheter
18	Eugene Ozhinsky	T2-Based Temperature Monitoring in Abdominal Fat during HIFU Treatment
19	Chia-Hung Sze	Development of an Intravascular Gentamicin Filter Device for High-Dose Drug Delivery
20	Mariam Aboian	Small scale fluorescence-based method for identifying chemotherapeutic binding to ChemoFilter resin.
21	Misung Han	T1-Based Thermometry in Cortical Bone by Using Ultrashort Echo-Time MRI
22	Parham Moftakhar	New Generation Endovascular Catheter for Interventional MRI
23	Aaron Losey	Magnetically Assisted Remote-controlled Catheter for MRI: Navigation at 1.5 T versus X-ray
24	Yong Pang	Investigation of the behavior of a volume coil array
25	Peter Shin	Chemical Shift Separation with Controlled Aliasing for Hyperpolarized 13C Metabolic Imaging

26	Jeremy Gordon	Application of Ramp-Sampled, Symmetric EPI to Dynamic Imaging of Hyperpolarized 13C Substrates
27	Hong Shang	Suppression of unwanted resonances in hyperpolarized MR studies with neat [1-13C]lactic acid
28	Sonam Iqbal	Sampling strategies for Dynamic Metabolic Imaging of Hyperpolarized 13 C Substrates
29	Nicole Wilson	Standardizing Radiation Dose for Computed Tomography Across the UC Medical Centers
30	Jack Lambert	Development of a Monte Carlo-based virtual CT scanner for pediatric dose calculation
31	Sant Kumar	Preclinical toxicity tests of novel enteric silicon CT contrast material
32	Jaewon Yang	The potential impact of external RF coils on PET/MR: A phantom study
33	Tanushree Ganguly	FDG- based prodrugs for imaging chemical microenvironment
34	Joseph Blecha	A New Approach to PET Labeling Norepinephrine Transporter Imaging Agents
35	Robert Flavell	Imaging the acidic prostate tumor microenvironment with 18F-FDG prodrugs and hyperpolarized 13C MRI
36	Christopher Drake	Imaging the Glucocorticoid Receptor in Castration-Resistant Prostate Cancer
37	Jeremy Bancroft Brown	RF Coil Design for Microscale Ex Vivo DWI of Prostate Biopsies at 14.1T
38	Olga Starobinets	Pilot: MRI Differences Associated with Anti-androgen Treatments in Low Risk Prostate Cancer Patients
39	David Korenchan	High-resolution pH Imaging Using Hyperpolarized 13C-Bicarbonate
40	Jessie Lee	Development of Hyperpolarized 13C Imaging Biomarkers for Prostate Tumor Ablation After HIFU Therapy
41	Llewellyn (Trey) Jalbert	MR Imaging / Spectroscopy Provides Insight into Malignant Transformation and IDH-mutation in Glioma
42	Natalie Korn	Semi-automatic Segmentation of the Prostate by MR Fat Fraction Map
43	Renuka Sriram	Measurement of hyperpolarized lactate production and efflux as a biomarker of tumor aggressiveness
44	Jose Izquierdo	13C MRS detects metabolic flux adaptation in IDH mutant glioma cells
45	Marina Radoul	Monitoring of GBM response to novel PI3K/mTOR inhibitors using hyperpolarized 13C MRSI and 1H MRS
46	Lisa Wilmes	Evaluating Variability in Quantitative Breast MRI Using Novel Phantom
47	David Newitt	Gradient nonlinearity correction to improve ADC accuracy in breast cancer clinical trials
48	Cindy Lee	An analysis of screening mammography performance in the National Mammography Database
49	Jessica Hayward	Screening Mammography Recall Rate: Effect of Multiple Prior Comparison Exams
50	Julia Nguyen	Characterization of Inflammation in Cell and Animal Models Using Hyperpolarized 13C-Pyruvate
51	Yiran Chen	A study of maturation in mice by the use of hyperpolarized 13C compounds
52	Hosung Kim	MRI volumetry reveals slower brain growth in preterm neonates with cerebellar hemorrhagic injury
53	Yi-Shin Chang	Changes of neurite density and fiber orientation dispersion during human brain maturation

54	Nico Papinutto	2D PSIR to measure in-vivo spinal cord GM and WM areas in clinically feasible acquisition times
55	Rachel Nosheny	BrainHealthRegistry.org: Implementing an online registry for clinical trials in UCSF Radiology Dept.
56	Eva M. Palacios	Towards Precision Neuroimaging: DTI Standardization of a Multicenter Traumatic Brain Injury Study
57	Susanne Mueller	Atrophy and Network Disruption in the Brainstem: A Risk Factor for SUDEP?
58	Olga Tymofiyeva	Can DTI network properties capture brain changes after 8 weeks of mindfulness-based therapy?
59	Donna Murray	Alterations in Frontal White Matter and Basal Ganglia Metabolite Levels in Alcohol Abstinence
60	Angela Jakary	7T DTI Characteristics of Mindfulness-Based Cognitive Therapy for Depression
61	Regina Schlaeger	Spinal cord gray matter atrophy correlates with multiple sclerosis disability
62	Carter H. Hultman	Magnetization Transfer Imaging of Spinal Cord Gray and White Matter in Multiple Sclerosis
63	Yu Zhang	Corticostriatal degeneration in Parkinson's disease and relations to cognitive and motor deficits
64	Caroline Niziolek	Internal vs. external deviations from auditory targets in speech
65	Marcel Brus-Ramer	18F-NaF PET Evaluation of Facet Joints of Lumbar Spine Compared with CT and MRI Graded Arthropathy
66	Marc Mabray	The Significance of Focal Parotid FDG Uptake on Whole Body PET Imaging